

A stable second-order partitioned iterative scheme for freely vibrating low-mass bluff bodies in a uniform flow

R.K. Jaiman*, N.R. Pillalamarri, M.Z. Guan

Department of Mechanical Engineering, National University of Singapore, Singapore 119077, Singapore

Received 1 May 2015; received in revised form 17 December 2015; accepted 18 December 2015

Available online 30 December 2015

Abstract

We present a stable partitioned iterative scheme for solving fluid–body interaction problems at low structure-to-fluid mass ratio. The scheme relies on the so-called nonlinear interface force correction based on Aitken’s extrapolation process to stabilize the coupled partitioned system employing an arbitrary Lagrangian–Eulerian finite element framework. Approximate interface force correction is constructed through subiterations to account for the missing effects of off-diagonal Jacobian terms in the partitioned staggered scheme. Through the generalized Aitken’s geometric extrapolation process with a dynamic stabilization parameter, the interface corrections allow to satisfy the force equilibrium with arbitrary accuracy while expanding the scope of partitioned iterative schemes for fluid–structure interaction with strong added-mass effects. To assess the proposed iterative scheme against the standard strong coupling, effects of mass ratio are investigated for a freely vibrating circular cylinder. We show that our second-order scheme is stable for low mass density ratio and hence is able to handle strong added-mass effects. The numerical stability and robustness of the scheme is then demonstrated for a new application of tandem square cylinder undergoing complex wake-induced vibration and galloping.

© 2015 Elsevier B.V. All rights reserved.

Keywords: Interface force correction; Added mass effects; Subiteration; Aitken’s process; Dynamic stabilization parameter; Wake-induced vibration

1. Introduction

Coupled dynamical fluid–structure systems exhibit a great variety of self-excited vibrations, both in useful and destructive manners. In particular, ocean environments are full of such self-excited vibrations, which constitute an interesting problem for the numerical modeling and can have a significant impact on the systems used in ocean and offshore engineering, including moorings, risers, subsea pipelines, large floating structures, and energy harvesting devices. In the dynamics of coupled fluid–body interaction, the phenomenon of frequency lock-in may occur for a given range of control parameters. The frequency of one system, e.g. fluid wake, deviates from its expected values

* Corresponding author.

E-mail address: mperk@nus.edu.sg (R.K. Jaiman).

while being close to the frequency of the another system, e.g. structure. In the absence of solid motion, the shedding frequency in the wake of a bluff body increases proportionally with the flow velocity according to the Strouhal law [1,2]. When the solid is let free to vibrate in cross-flow direction, a strong non-linear coupling between the motion and the wake dynamics exists. This results in a complex evolution of the shedding frequency which deviates from the Strouhal law as the natural frequency of the structure is approached, which is referred to as a lock-in of the wake frequency to the structural frequency. The lock-in range corresponds to a large amplitude oscillatory motion of the bluff body, which is of a practical importance in offshore and marine structures [3,4].

In the case of vortex-induced vibration, the frequency of unstable wake system approaches that of the oscillating bluff body which leads to an oscillating lift force with increasing amplitude of motion through a nonlinear resonance shift. The peak amplitudes and extent of lock-in, in terms of reduced velocity, is known to be significantly affected by the mass ratio between the structure and fluid systems. The upper limit of the extent of lock-in increases as the mass ratio from structure to fluid is decreased, which has been confirmed through experimental and theoretical studies. The authors [5,6] experimentally studied 2-DOF VIV of a circular cylinder at low mass ratios and reported a new response branch the so-called super-upper branch, which occurs when the mass ratio $m^* \leq 6$ in the turbulent regime. The peak vibration amplitude in the super-upper branch can go up to 1.5 times of the cylinder diameter.

For modeling the interaction of fluid flow with vibrating structures, ALE based simulations are generally accomplished by using either partitioned or monolithic schemes. A monolithic [7–10] approach assembles the fluid and structural equations into a single block and solves them simultaneously for each iteration. The fully-coupled finite-element formulation and implementation are discussed in details in [10]. The kinematic compatibility at the interface is achieved by construction, which leads to a reduction in the size of the linear system solved per nonlinear iteration. These schemes lack the advantage of flexibility and modularity of using existing stable fluid or structural solvers. However, they offer good numerical stability even for problems involving very strong added mass effects. In contrast, a partitioned approach solves the fluid and structural equations in a sequential manner, facilitating the coupling of the existing fluid and structural program with minimal changes. This trait renders the partitioned approach an attractive option from the computational point of view.

Typically, partitioned staggered schemes [11] are classified as either strongly-coupled (implicit) [12] or loosely-coupled [13,14]. Loosely-coupled (explicit) schemes satisfy the interface velocity continuity and traction continuity conditions in a sequential manner. These schemes often suffer from numerical instability and temporal inaccuracy caused by spurious energy production along the interface due to the time lag [15,16], and special treatments are generally required to address these issues. The numerical instability depends upon the material properties of fluid and structure and also on the relative geometric scales of the domain and the compressibility of the fluid. Notably, the sequential staggering introduces an explicit nature into the coupling even if both domains are solved implicitly. For an incompressible fluid interacting with low mass structures, reducing the time step size does not cure the instability regardless of whether the Courant condition for the individual domain is satisfied. This implies the instability is inherent in the sequential staggered scheme due to the strong nature of fluid–structure coupling [17–19]. A variety of force corrections and structural predictors [13,20] are used to increase the numerical stability of loosely-coupled schemes. Strongly-coupled schemes typically involve predictor–corrector subiterations to ensure the convergence of interface properties [21,22].

In several applications such as flow through blood vessels [18], ocean current interactions with offshore risers [23], strongly-coupled schemes suffer from convergence issues due to strongly predominant added mass effects. Theoretical closed-form findings of added mass force in [19,24] have clearly illustrated the difference between compressible and incompressible flow interacting with oscillating structure. For a model elastic plate, the added mass of a compressible flow system is proportional to the length of time interval, whereas the added mass of an incompressible system asymptotically approaches a constant value as the length of the time interval goes to zero. This finding has an implication in the design of fluid–structure coupling algorithms and the stability and convergence properties of the subiterations [25,23,17,21,18]. For large-scale FSI simulations, it is important to develop an efficient and general approach towards solving fluid flows coupled with flexible multibody dynamical structures. The flows can be modeled as fully incompressible or slightly compressible and can include turbulence effects. The structural components can comprise rigid bodies, solids, shells, beams and other elements including contact surfaces, gaps etc. For such large-scale flexible multibody dynamic interactions, monolithic formulations may require a substantial amount of effort and restructuring of the fluid and solid codes. On the other hand, partitioned procedures have desirable properties with regard to software developments, scalability and parallel processing.

This paper presents a novel ALE based fluid–structure interaction method to couple existing fluid and structure solvers. In particular, we are interested in simulations of offshore applications involving low-mass bluff bodies such as tandem cylinders and offshore floating structure subjected to vortex-induced vibrations. A solver using Petrov–Galerkin finite-element and semi-discrete time stepping has been developed to investigate the hydrodynamic characteristics around vibrating circular and square cylinders. Identical order of interpolation has been used for the primitive variables, which implies their collocated arrangement at discrete nodes. The formulation used in this work is referred to as the streamline-upwind Petrov–Galerkin method (SUPG) [26,27], which in the framework of linear finite element interpolation, may be regarded as a Galerkin/least-squares stabilization technique [28]. To account for fluid–body interaction, a partitioned iterative scheme the so-called nonlinear interface force correction (NIFC) has been developed. The temporal discretization of both the fluid and the structural equations is embedded in the generalized- α framework by making use of classical Newmark approximations in time [29,8].

Our objective is to present a partitioned iterative scheme that couples structure, ALE and fluid fields in a staggered fashion. The fields are advanced explicitly and the interface force correction is constructed at the end of each fluid subiteration to account for the missing off-diagonal Jacobian terms. Through the fully implicit scheme, we not only achieve the coupled fluid–structure stability for low structure-to-fluid mass ratio but also the coupled solver is stable for a large time step size. To satisfy the force equilibrium while maintaining the velocity continuity condition along the fluid–structure interface, approximate interface force correction is formed as an iterative sequence through subiterations and the generalized Aitken’s iterated Δ^2 process with a dynamic relaxation parameter. Our key idea is to construct the dynamic sequence parameter for stabilizing the interface force along fluid–structure interface. We demonstrate that the geometric extrapolations with the nonlinear iterative force correction can provide an interesting and practical possibility to transform a divergent force sequence to a stable and convergent sequence for fluid–structure interaction with strong added-mass effects. We show the second-order temporal accuracy for a test problem of vibrating square cylinder and verify the precision of the NIFC scheme with the available results. We compare the stability of the transformed force update sequence with the untransformed block-iterative sequence for a freely vibrating cylinder at low-mass ratio. We demonstrate the methodology for a new application of flow-induced vibration of tandem square cylinder undergoing combined wake-induced and galloping instabilities.

The outline of the rest of the article is as follows. The governing equations for fluid–body system and its finite-element and a review of partitioned staggered methods are discussed in Sections 2 and 3, respectively. In Section 4, we present the nonlinear interface force correction procedure based on a generalized Aitken’s extrapolation process. Accuracy of the computations and convergence of results are presented in Section 5, whereas the effects of mass-ratio have been investigated in Section 6. In Section 7, we present an application of paired bluff bodies to study the combined wake-induced vibration and galloping of a tandem square cylinder. The major conclusions of this work are reported in Section 8.

2. Numerical formulation

In this section, we present a coupled fluid–body solver for rigid-body dynamics based on the NIFC formulation. The rigid-body dynamics for low mass-ratios using traditional numerical techniques such as loosely-coupled and strongly-coupled partitioned staggered schemes may suffer from numerical instabilities and convergence related issues, respectively [18,25]. For the sake of completeness, we first present the coupled equations and a semi-discrete Petrov–Galerkin formulation of the fluid–body solver. Later we summarize the NIFC formulation in a coupled fluid–structure matrix form.

2.1. The governing equations for flow and rigid body motion

The governing equations for the fluid are written in an arbitrary Lagrangian–Eulerian (ALE) form while the structural equation is formulated in a Lagrangian way. The Navier–Stokes equations for an incompressible flow in an ALE frame are

$$\rho^f \left(\frac{\partial \mathbf{u}^f}{\partial t} \Big|_{\hat{\mathbf{x}}} + (\mathbf{u}^f - \mathbf{w}) \cdot \nabla \mathbf{u}^f \right) = \nabla \cdot \boldsymbol{\sigma}^f + \mathbf{b}^f \quad \text{on } \Omega^f(t), \quad (1)$$

$$\nabla \cdot \mathbf{u}^f = 0 \quad \text{on } \Omega^f(t), \quad (2)$$

where $\mathbf{u}^f = \mathbf{u}^f(\mathbf{x}, t)$ and $\mathbf{w} = \mathbf{w}(\mathbf{x}, t)$ represent the fluid and mesh velocities defined for each spatial point $\mathbf{x} \in \Omega^f(t)$, respectively. In Eq. (1), the partial time derivative with respect to the ALE referential coordinate $\hat{\mathbf{x}}$ is kept fixed. The spatial derivatives are taken with respect to the current spatial coordinates denoted by \mathbf{x} . The body force per unit mass applied on the fluid is \mathbf{b}^f and $\boldsymbol{\sigma}^f$ is the Cauchy stress tensor for a Newtonian fluid, written as

$$\boldsymbol{\sigma}^f = -p^f \mathbf{I} + \mu^f \left(\nabla \mathbf{u}^f + \left(\nabla \mathbf{u}^f \right)^T \right) \quad (3)$$

where p^f denotes the fluid pressure and μ^f is the dynamic viscosity of the fluid.

A rigid-body structure immersed in the fluid experiences unsteady fluid forces and consequently may undergo flow-induced vibrations if mounted elastically. The rigid-body motion along the Cartesian axes is governed by the following equation:

$$\mathbf{m} \cdot \frac{\partial \mathbf{u}^s}{\partial t} + \mathbf{c} \cdot \mathbf{u}^s + \mathbf{k} \cdot (\boldsymbol{\varphi}^s(\mathbf{z}_0, t) - \mathbf{z}_0) = \mathbf{F}^s + \mathbf{b}^s \quad \text{on } \Omega^s, \quad (4)$$

where \mathbf{m} , \mathbf{c} and \mathbf{k} denote the mass, damping and stiffness vectors per unit length for the translational degrees of freedom, Ω^s denotes the rigid body, $\mathbf{u}^s(t)$ represents the rigid-body velocity at time t as

$$\mathbf{u}^s(\mathbf{z}_0, t) = \frac{\partial \boldsymbol{\varphi}^s}{\partial t} \quad (5)$$

where $\boldsymbol{\varphi}^s$ denotes the position vector mapping the initial position \mathbf{z}_0 of the rigid body to its position at time t , and \mathbf{F}^s and \mathbf{b}^s are the fluid traction and body forces acting on the rigid body, respectively. The solid body is rotationally constrained and thereby the conservation of angular momentum and the velocity corresponding to the rotations can be ignored. The fluid and the structural equations are coupled by the continuity of velocity and traction along the fluid–structure interface.

Let $\Gamma_{fs} = \partial\Omega^f(0) \cap \partial\Omega^s$ be the fluid–structure interface at $t = 0$ and $\Gamma_{fs}(t) = \boldsymbol{\varphi}^s(\Gamma_{fs}, t)$ is the fluid–structure interface at time t . The coupled system requires to satisfy the continuity of velocity and traction at the fluid–body interface Γ_{fs} as follows

$$\mathbf{u}^f(\boldsymbol{\varphi}^s(\mathbf{z}_0, t), t) = \mathbf{u}^s(\mathbf{z}_0, t), \quad (6)$$

$$\int_{\boldsymbol{\varphi}^s(\gamma, t)} \boldsymbol{\sigma}^f(\mathbf{x}, t) \cdot \mathbf{n} d\Gamma(\mathbf{x}) + \int_{\Gamma} \mathbf{F}^s d\Gamma = 0, \quad (7)$$

where \mathbf{n} is the outer normal to the fluid–body interface, γ is any part of the fluid–body interface Γ_{fs} in the reference configuration, $d\Gamma$ denotes a differential surface area and $\boldsymbol{\varphi}^s(\gamma, t)$ is the corresponding fluid part at time t . In Eq. (7), the first term represents the force exerted by the fluid on $\boldsymbol{\varphi}^s(\gamma, t)$, while the second term represents the net force by the rigid body on $\boldsymbol{\varphi}^s(\gamma, t)$.

2.2. Weak form of fluid–rigid body system

The weak form of the Navier–Stokes equations (1) and (2) can be written as

$$\begin{aligned} & \int_{\Omega^f(t)} \rho^f \left(\partial_t \mathbf{u}^f + (\mathbf{u}^f - \mathbf{w}) \cdot \nabla \mathbf{u}^f \right) \cdot \boldsymbol{\phi}^f(\mathbf{x}) d\Omega + \int_{\Omega^f(t)} \boldsymbol{\sigma}^f : \nabla \boldsymbol{\phi}^f(\mathbf{x}) d\Omega \\ &= \int_{\Omega^f(t)} \mathbf{b}^f \cdot \boldsymbol{\phi}^f(\mathbf{x}) d\Omega + \int_{\Gamma_{fs}^f(t)} \mathbf{h}^f \cdot \boldsymbol{\phi}^f(\mathbf{x}) d\Gamma + \int_{\Gamma(t)} \left(\boldsymbol{\sigma}^f(\mathbf{x}, t) \cdot \mathbf{n}^f \right) \cdot \boldsymbol{\phi}^f(\mathbf{x}) d\Gamma, \end{aligned} \quad (8)$$

$$\int_{\Omega^f(t)} \nabla \cdot \mathbf{u}^f q(\mathbf{x}) d\Omega = 0. \quad (9)$$

Here ∂_t denotes partial time derivative operator $\partial(\cdot)/\partial t$, $\boldsymbol{\phi}^f$ and q are test functions for the fluid velocity and pressure, respectively. $\Gamma_{fs}^f(t)$ represents the non-interface Neumann boundary along which $\boldsymbol{\sigma}^f(\mathbf{x}, t) \cdot \mathbf{n}^f = \mathbf{h}^f$. The weak form for

the rigid-body equation (4) is

$$\int_{\Omega^s} [\mathbf{m} \cdot \partial_t \mathbf{u}^s + \mathbf{c} \cdot \mathbf{u}^s + \mathbf{k} \cdot (\boldsymbol{\varphi}^s(\mathbf{z}_0, t) - \mathbf{z}_0)] \cdot \boldsymbol{\phi}^s d\Omega = \int_{\Gamma} \mathbf{F}^s \cdot \boldsymbol{\phi}^s d\Gamma + \int_{\Omega^s} \mathbf{b}^s \cdot \boldsymbol{\phi}^s d\Omega, \quad (10)$$

where $\boldsymbol{\phi}^s$ is the test function for the rigid-body velocity, which is a constant for any point on the body. Similarly, we can write the weak form for the traction boundary condition as

$$\int_{\varphi(\gamma, t)} (\boldsymbol{\sigma}^f(\mathbf{x}, t) \cdot \mathbf{n}) \cdot \boldsymbol{\phi}^f d\Gamma + \int_{\gamma} \mathbf{F}^s \cdot \boldsymbol{\phi}^s d\Gamma = 0. \quad (11)$$

One may observe that the fluid and structural velocities, and their test functions, respectively, are defined on different domains $\Omega^f(t)$ and Ω^s , and satisfy the matching condition along the interface

$$\boldsymbol{\phi}^f(\mathbf{x}) = \boldsymbol{\phi}^s(\mathbf{z}_0), \quad (12)$$

where $\mathbf{x} = \boldsymbol{\varphi}^s(\mathbf{z}_0, t)$ with $\boldsymbol{\varphi}^s$ being the position vector of the solid.

The characterization of the moving fluid–body interface is constructed by means of the ALE technique [30,31]. The movement of the internal finite-element nodes is achieved by solving the hyperelastic model for fluid mesh such that the mesh quality does not deteriorate as the displacement of the rigid body increases. For the sake of completeness, we next present a semi-discrete formulation using a standard Petrov–Galerkin procedure [32] with equal order interpolation for velocity and pressure.

2.3. Semi-discrete Petrov–Galerkin formulation

The spatial domain Ω^f is partitioned into the non-overlapping finite elements Ω^e , $e = 1, 2, \dots, n_{el}$, where n_{el} is the number of elements. We adopt a generalized- α method to integrate in time between $t \in [t^n, t^{n+1}]$, which can be unconditionally stable and second-order accurate for linear problems [29,33]. The scheme enables user-controlled high frequency damping, which is desirable for a coarser discretization in space and time. This is achieved by specifying a single parameter the so-called spectral radius, ρ_∞ . The time-derivatives of fluid and structure unknowns are evaluated at the generalized midpoint α_m^i , while the expressions of the unknowns are evaluated at α^i , with $0 \leq \alpha_m^i \leq 1$ and $0 \leq \alpha^i \leq 1$ where $i = f, s$. This algorithm dampens the spurious high-frequency responses, but retains the second-order accuracy.

With the aid of the generalized- α parameters ($\alpha^f, \alpha_m^f, \alpha^s, \alpha_m^s$), the coupled variational fluid–rigid body formulation along with the residual stabilization terms can be written as follows

$$\begin{aligned} & \int_{\Omega_h^f(t^{n+1})} \rho^f \left(\partial_t \mathbf{u}_h^{f, n+\alpha_m^f} + \left(\mathbf{u}_h^{f, n+\alpha^f} - \mathbf{w}_h^{n+\alpha^f} \right) \cdot \nabla \mathbf{u}_h^{f, n+\alpha^f} \right) \cdot \boldsymbol{\phi}^f d\Omega \\ & \quad + \int_{\Omega_h^f(t^{n+1})} \boldsymbol{\sigma}_h^{f, n+\alpha^f} : \nabla \boldsymbol{\phi}^f d\Omega \\ & \quad - \int_{\Omega_h^f(t^{n+1})} \nabla \cdot \mathbf{u}_h^{f, n+\alpha^f} q d\Omega \\ & \quad + \sum_{e=1}^{n_{el}} \int_{\Omega^e} \tau_m \left(\rho^f \left(\mathbf{u}_h^{f, n+\alpha^f} - \mathbf{w}_h^{n+\alpha^f} \right) \cdot \nabla \boldsymbol{\phi}^f + \nabla q \right) \cdot \left(\rho^f \mathbf{u}_t^{f, n+\alpha_m^f} \right. \\ & \quad \left. + \rho^f \left(\mathbf{u}_h^{f, n+\alpha^f} - \mathbf{w}_h^{n+\alpha^f} \right) \cdot \nabla \mathbf{u}_h^{f, n+\alpha^f} - \nabla \cdot \boldsymbol{\sigma}_h^{f, n+\alpha^f} - \mathbf{f}^f(t^{n+\alpha^f}) \right) d\Omega^e \\ & \quad + \sum_{e=1}^{n_{el}} \int_{\Omega^e} \nabla \cdot \boldsymbol{\phi}^f \tau_c \rho^f \nabla \cdot \mathbf{u}_h^{f, n+\alpha^f} d\Omega^e \\ & \quad + \int_{\Omega^s} \left[\mathbf{m} \cdot \partial_t \mathbf{u}_h^{s, n+\alpha_m^s} + \mathbf{c} \cdot \mathbf{u}_h^{s, n+\alpha^s} + \mathbf{k} \cdot \left(\boldsymbol{\varphi}_h^{s, n+\alpha^s}(\mathbf{z}_0) - \mathbf{z}_0 \right) \right] \cdot \boldsymbol{\phi}^s d\Omega \\ & = \int_{\Omega_h^f(t^{n+1})} \mathbf{b}^f(t^{n+\alpha^f}) \cdot \boldsymbol{\phi}^f d\Omega + \int_{\Gamma_h^f(t^{n+1})} \mathbf{h}^f \cdot \boldsymbol{\phi}^f d\Gamma + \int_{\Omega^s} \mathbf{b}^s(t^{n+\alpha^s}) \cdot \boldsymbol{\phi}^s d\Omega, \end{aligned} \quad (13)$$

where the lines 4, 5 and 6 represent the stabilization terms applied on each element locally and the remaining terms with the right-hand side constitute the Galerkin terms of the variational fluid–body problem. The stabilization parameters τ_m and τ_c appearing in the element level integrals are the least-squares metrics added to the fully discretized formulation. The least-squares metric τ_m for the momentum equations is defined as

$$\tau_m = \left[\left(\frac{2\rho^f}{\Delta t} \right)^2 + (\rho^f)^2 (\mathbf{u}_h^f - \mathbf{w}_h) \cdot \mathbf{G} (\mathbf{u}_h^f - \mathbf{w}_h) + C_I (\mu^f)^2 \mathbf{G} : \mathbf{G} \right]^{-\frac{1}{2}}, \quad (14)$$

where C_I is the constant coming from the element-wise inverse estimate [34] and \mathbf{G} is the size of element contravariant metric tensor [8,35]. The contravariant metric can be defined as

$$\mathbf{G} = \frac{\partial \xi^T}{\partial \mathbf{x}} \frac{\partial \xi}{\partial \mathbf{x}}, \quad (15)$$

where \mathbf{x} and ξ are the physical coordinates and parametric counterpart, respectively. The least-squares metric τ_c for the continuity equation is defined as

$$\tau_c = \frac{1}{\text{tr} \mathbf{G} \tau_m} \quad (16)$$

where $\text{tr} \mathbf{G}$ denotes the trace of the contravariant metric tensor. The stabilization treatment serves two purposes: First, it provides stability to the velocity field in convection dominated regions of the fluid domain. Second, it circumvents the Babuska–Brezzi condition, which any standard mixed Galerkin method has to satisfy [32]. The definition of metric τ_m is the crucial component which provides the appropriate combination of stability and accuracy. The element metric tensor \mathbf{G} intrinsically deals with different element topology for different mesh discretizations. This metric has been greatly studied in the literature [36,37,32,38,39] of stabilized finite element formulation for the Navier–Stokes equations. Next we present a brief review of partitioned framework to motivate for the development of NIFC.

3. Review of partitioned FSI framework

The coupled fluid–structure interaction equations comprise the initial–boundary value problems of the fluid and the structure, complemented by the traction (dynamic) and displacement (kinematic) boundary conditions at the fluid–structure interface. In the partitioned approach, the decomposed domains of the fluid and solid share a common interface boundary. The structural equations are conventionally formulated in Lagrangian coordinates on a mesh that moves along with the material, while the fluid equations are formulated in Eulerian coordinates, where the mesh serves as a fixed reference for the fluid motion. For the coupling of these media, the fluid solutions conform to the structural motion by the ALE formulation. Particular care must be taken to properly couple the fluid and the structure along the interface between the media and the underlying interface discretizations [40].

At each time step, explicit staggered techniques are generally used to satisfy the continuity of velocity and traction conditions in a sequential manner, often referred to as the conventional sequential staggered (CSS) procedure [11]. The explicit CSS scheme appears to be attractive from a computational viewpoint as the solutions of the fluid and the structures are computed once per time step. However, it may suffer significantly from destabilizing effects introduced due to a lag between the fluid and structure solutions [18,17,25,22]. Depending on the direction of the interface acceleration, high under- or over-prediction of pressure may occur due to the lack of energy equilibrium across the fluid–structure interface. In other words, any small error in the interface displacements imposed onto the fluid by the structure will result in large errors in fluid pressure. The effect of the added mass pertaining to incompressible flows on the convergence and stability of partitioned solution methods has recently been investigated in [19,18,17].

A variety of structural predictors and force corrections can be employed at each time step to enhance the coupled numerical stability, for example: generalized sequential staggered (GSS) [14] and combined-interface boundary conditions [13,41,42]. At each time step, the prediction of displacement and the correction of forces are formed in a sequential manner along the fluid–structure interface, the velocity prediction:

$$\mathbf{u}_f^P = \mathbf{u}_s + \delta \mathbf{u}_* \quad \text{on } \Gamma_{fs} \quad (17)$$

and traction correction as

$$\mathbf{P}_s^C = \mathbf{P}_f + \delta \mathbf{P}_* \quad \text{on } \Gamma_{fs} \quad (18)$$

where the velocity prediction $\delta \mathbf{u}_*$ and the force correction $\delta \mathbf{P}_*$ terms are explicit functions of spatial and temporal solutions: traction, velocity and acceleration of fluid and structure along the interface [13]. These interface prediction and correction terms are only applied to the right hand side of fluid and structure equations at two consecutive time instants. The CIBC correction terms [13,41,43] can be given as

$$\delta \mathbf{P}_* = -\frac{\Delta t}{\omega} \left(\frac{\partial p^f}{\partial n} \mathbf{n} + \rho_f \frac{\partial \mathbf{u}^s}{\partial t} \right) \quad (19)$$

$$\delta \mathbf{u}_* = \Delta t \left(-\frac{\partial p^f}{\partial n} \mathbf{n} + \omega \frac{\partial (\delta \mathbf{P}_*)}{\partial t} \right) \quad (20)$$

where ω is the coupling parameter and can be chosen as $\omega/\Delta t = O(100)$ for a stable and accurate solution [42,43]. The integral form of the traction correction along the fluid–structure interface can be written as

$$\int_{\Gamma} \delta \mathbf{P}_* d\Gamma = -\frac{\Delta t}{\omega} \left(\int_{\Gamma} \frac{\partial p^f}{\partial n} \mathbf{n} d\Gamma + \rho_f \frac{\partial \mathbf{u}^s}{\partial t} S \right) \quad (21)$$

where $S = \int_{\Gamma} d\Gamma$ is the surface area. The structural traction term in the velocity correction can be eliminated with some modifications in the original CIBC formulation [41]. The CIBC terms can further accelerate the subiteration process in the partitioned implicit coupling algorithm.

The above predictor–corrector procedure generally determines the order of temporal accuracy and provides an interface based relaxation to the coupled numerical instability. In addition, the explicit correction terms involve coupling parameter and coefficients which depend on the underlying spatial discretization and the time integration schemes. Recently, several partitioned solution methods based on the subiteration as a component have been proposed to address this class of problems. A recent review of partitioned iterative schemes has been provided in [22]. For coupled problems with strong added-mass effects, the brute-force subiterations can be unstable or they can be very slow in the convergence. In [22], the analysis of subiteration-based partitioned techniques include the modified-mass method [44] and standard underrelaxation, Aitken’s extrapolation [45], interface-GMRES and interface-Krylov methods [46,47]. In the next section, we turn our attention to the iterative force correction scheme based on the subiterations and a generalized Aitken’s extrapolation process. We next present the coupled algebraic system of fluid–structure equations. For a partitioned treatment of coupled fluid–structure interaction problems, it is a customary to devise the field-specific discretizations and solution procedures for the decomposed sub-domains. The coupled system can be independently discretized with the aid of suitable and desired types of formulations for fluid and structural sub-domains.

4. Interface force correction scheme

The resulting coupled algebraic system of fluid–structure equations to be solved for each time step can be written in abstract form:

$$\begin{bmatrix} \mathbf{A}_{11} & 0 & 0 & \mathbf{A}_{14} \\ \mathbf{A}_{21} & \mathbf{A}_{22} & 0 & 0 \\ 0 & \mathbf{A}_{32} & \mathbf{A}_{33} & 0 \\ 0 & 0 & \mathbf{A}_{43} & \mathbf{A}_{44} \end{bmatrix} \begin{Bmatrix} \Delta \boldsymbol{\varphi}_s \\ \Delta \boldsymbol{\varphi}_I \\ \Delta \mathbf{q}_f \\ \Delta \mathbf{f}_I \end{Bmatrix} = \begin{Bmatrix} \mathbf{R}_1 \\ \mathbf{R}_2 \\ \mathbf{R}_3 \\ \mathbf{R}_4 \end{Bmatrix} \quad (22)$$

where $\boldsymbol{\varphi}_s$ denotes structural displacement, \mathbf{q}_f denotes fluid variables, pressure, velocity and ALE motion solution fields. Since we define additional interface fields satisfying the continuity of tractions and displacements, $\boldsymbol{\varphi}_I$ and \mathbf{f}_I denotes interface displacement and force vector, respectively. The right-hand vectors \mathbf{R}_1 and \mathbf{R}_3 represent equation systems for the structural and fluid models; and \mathbf{R}_2 and \mathbf{R}_4 denote the imbalances (residual error) in the kinematic compatibility and dynamic equilibrium conditions.

The derivatives of fluid, solid and interface equations (Jacobian matrices) with respect to the state variables are given by the left-hand side matrix \mathbf{A} . Notably, \mathbf{A}_{21} is an extraction matrix which maps from the solid to the interface,

A_{43} is the force computation and the mapping to the interface and A_{22}, A_{44} are identity matrices. A_{11} denotes structure stiffness matrix, A_{32} connects the displacement condition through the ALE mapping, and A_{14} gets solid load vector from the computed interface forces [48]. A_{33} denotes the coupled fluid velocity/pressure linear system arising from the linearization of the discrete continuity and momentum equations. This linear system may be written as

$$\begin{bmatrix} \mathbf{K} & \mathbf{G} \\ -\mathbf{G}^T & \mathbf{C} \end{bmatrix} \begin{Bmatrix} \Delta \mathbf{U} \\ \Delta \mathbf{P} \end{Bmatrix} = \begin{Bmatrix} \mathbf{R}_m \\ \mathbf{R}_c \end{Bmatrix} \quad (23)$$

where \mathbf{K} is stiffness matrix of the momentum equation, which includes the inertia, convection, diffusion, source and stabilizing terms; \mathbf{G} is the discrete gradient operator; \mathbf{G}^T is the divergence operator; \mathbf{C} is the pressure–pressure stabilization term; $\Delta \mathbf{U}$ and $\Delta \mathbf{P}$ are the nodal velocity and pressure increments; and \mathbf{R}_m and \mathbf{R}_c are the discrete residual of the momentum and continuity equations. A_{34} represents the linearization of the Navier–Stokes system with respect to the interface force increment $\Delta \mathbf{f}_I$.

4.1. Static condensation of coupled block matrix

The idea now is to eliminate the off-diagonal term A_{14} through the static condensation (Schur complement) procedure and to obtain the following matrix form for the staggered cycle:

$$\begin{bmatrix} A_{11} & 0 & 0 & 0 \\ A_{21} & A_{22} & 0 & 0 \\ 0 & A_{32} & A_{33} & 0 \\ 0 & 0 & A_{43} & \tilde{A}_{44} \end{bmatrix} \begin{Bmatrix} \Delta \phi_s \\ \Delta \phi_I \\ \Delta \mathbf{q}_f \\ \Delta \mathbf{f}_I \end{Bmatrix} = \begin{Bmatrix} \mathbf{R}_1 \\ \mathbf{R}_2 \\ \mathbf{R}_3 \\ \tilde{\mathbf{R}}_4 \end{Bmatrix} \quad (24)$$

Using the static condensation, we have from the first row of (24)

$$A_{11} \Delta \phi_s = \mathbf{R}_1 - A_{14} \Delta \mathbf{f}_I. \quad (25)$$

Then by combining (25) and the second row, we obtain

$$A_{22} \Delta \phi_I = \mathbf{R}_2 - A_{21} (A_{11}^{-1} (\mathbf{R}_1 - A_{14} \Delta \mathbf{f}_I)). \quad (26)$$

Eq. (26) and the third row yield

$$A_{33} \Delta \mathbf{q}_f = \mathbf{R}_3 - A_{32} (A_{22}^{-1} (\mathbf{R}_2 - A_{21} (A_{11}^{-1} (\mathbf{R}_1 - A_{14} \Delta \mathbf{f}_I)))). \quad (27)$$

From the fourth row of force equilibrium condition with algebraic arrangements, we obtain:

$$\underbrace{(A_{44} - A_{43} A_{33}^{-1} A_{32} A_{22}^{-1} A_{21} A_{11}^{-1} A_{14})}_{\tilde{A}_{44}} \Delta \mathbf{f}_I = \underbrace{\mathbf{R}_4 - A_{43} A_{33}^{-1} (\mathbf{R}_3 - A_{32} A_{22}^{-1} (\mathbf{R}_2 - A_{21} A_{11}^{-1} \mathbf{R}_1))}_{\tilde{\mathbf{R}}_4}. \quad (28)$$

In the partitioned staggered procedure, there is no explicit availability of the Jacobian matrices entered in the Eq. (28). The interface force correction terms can be formed by iterating between the solutions of fluid and structure. In the nonlinear iterative force correction, we arrive at the iterative scheme of the following format

$$\Delta \mathbf{f}_I = \tilde{A}_{44}^{-1} \tilde{\mathbf{R}}_4 \quad (29)$$

the force correction vector $\tilde{A}_{44}^{-1} \tilde{\mathbf{R}}_4$ at the k th subiteration can be constructed by successive approximation (without explicitly forming A_{44} and its inverse), which essentially provides the approximated linearized fluid equation effects along the fluid–structure interface (Steklov–Poincaré operator). The off-diagonal terms are not explicitly formed in the scheme similar to [47]. Instead, the scheme proceeds in a similar fashion as the above predictor–corrector schemes by constructing an iterative interface force correction at each subiteration. As opposed to the CIBC formulation [49] for explicit staggered coupling, the implicit NIFC approach computes the dynamic stabilization parameter with the aid of subiterations between fluid and solid equations.

4.2. Approximate interface force

The development of NIFC scheme relies on the error decay or eigenvalue control where the brute-force subiterations perform poorly and lead to severe numerical instabilities for vibrating structure with strong added-mass effects. The evaluation of interface force can be considered as a generalization of Aitken's Δ^2 extrapolation scheme [50,51], with an idea to stabilize the iterative interface force sequence generated through the nonlinear iterations between fluid and structure. A new vector sequence transformation having a generalized kernel of the Aitken's Δ^2 process is constructed within the fixed-point iterative process. The key feature of our new implementation is the dynamic estimation of a stabilization sequence from the error amplification or eigenvalue analysis. Let f_I^0 be the initial estimate of force while f_I^* is the true solution, then initial force residual vector ΔE^0 can be written as:

$$\Delta E^0 = f_I^0 - f_I^* \quad (30)$$

and the difference between consecutive iterations

$$\Delta E^k = f_I^{k+1} - f_I^k \quad (31)$$

$$f_I^k = f_I^* + \tilde{A}_{44}^{-1} \tilde{R}_4^k \quad (32)$$

with the assumption of linearity property for the interface difference operator. For the iterative solution of interface force, we consider the power method for the above matrix eigenvalue problem and assume an $N \times N$ iteration matrix M is diagonalizable in the sense $Mv_k = \lambda_k v_k$ for each k and the eigenvalues λ_k are distinct and nonzero with corresponding eigenvectors v_k . With the help of the iteration matrix M and the error vector ΔE^0 , the force value can be written at the k th iteration as the matrix–vector product:

$$f_I^k = f_I^* + M^k \Delta E^0 \quad (33)$$

which can be further expressed using the consecutive estimates

$$f_I^k = f_I^0 + \sum_{i=0}^{k-1} M^i \Delta E^0, \quad k = 2, 3, \dots \quad (34)$$

From the error amplification analysis [52,53] and assuming the power-iteration series can be expressed as a linear combination of the eigenvectors v_i , the error vectors ΔE can be written

$$\Delta E_0 = f_1 - f_0 = \sum_{i=1}^N c_i v_i \quad (35)$$

$$\Delta E_1 = \sum_{i=1}^N c_i \lambda_i v_i \quad (36)$$

$$\Delta E_k = \sum_{i=1}^N c_i (\lambda_i)^k v_i \quad (37)$$

$$\Delta E_{k+1} = \sum_{i=1}^N c_i (\lambda_i)^{k+1} v_i. \quad (38)$$

The largest eigenvalue of the matrix can be expressed as

$$\lambda_1 = \lim_{k \rightarrow \infty} \left(\frac{\Delta E_{k+1}}{\Delta E_k} \right) \quad (39)$$

$$\lambda_1 \approx \left(\frac{\Delta E_{k+1}}{\Delta E_k} \right) \quad (40)$$

and the approximation of λ_1 can be constructed from the ratio of error differences at the k th iteration. To control the dominant eigenvalue adaptively, we introduce a dynamic stabilization parameter α_k at the k th iteration as:

$$\Delta \tilde{\mathbf{E}}_k = \alpha_k \Delta \mathbf{E}_k \quad (41)$$

and then we obtain for the force difference formula as the sequence of transformation:

$$\mathbf{f}_I^k - \mathbf{f}_I^0 = \frac{\alpha_k \Delta \tilde{\mathbf{E}}_k}{\|\Delta \tilde{\mathbf{E}}_k - \alpha_k \Delta \mathbf{E}_{k+1}\|} \quad (42)$$

which can be expressed as

$$\mathbf{f}_I^k - \mathbf{f}_I^0 = \gamma_k \Delta \tilde{\mathbf{E}}_k. \quad (43)$$

Setting the auxiliary sequence $\alpha_k = 1$ for all k , the above formulation recovers to the standard Aitken's iterated Δ^2 process with $\gamma_k = (1 - \lambda_k)^{-1}$ where γ_k is a continuous function in the neighborhood of λ_k and $\lambda_k \neq 1$. Iterative process based on the fixed-point iteration is known to build a function sequence that are diminishing in the form of geometric series [50,52,53]. Some generalizations of Aitken's extrapolation algorithms are given for several mathematical sequences in [54,55,51]. Detailed steps of the geometric extrapolations and the relationship with the interface force correction are given in [Appendix A](#).

The present force correction scheme can be considered as a generalization of Aitken's extrapolation with the aid of dynamic updating of stabilization sequence α_k . The geometric extrapolations with the dynamic eigenvalue control can provide an interesting and practical possibility to transform a divergent fixed-point iteration to a stable and convergent iteration. In general, the ability to extrapolate and dynamically control the solution sequence expands the scope of application of fixed-point iteration for fluid–structure interaction with strong added-mass effects. The inspiration of this stabilization parameter comes from the CIBC scheme whereby there is a need of the explicit coupling parameter for the traction correction. On the other hand, the NIFC procedure computes the force control parameter with minimum two subiterations between fluid and solid equations.

4.3. Implementation and algorithm

We now apply the nonlinear iterative sequence to estimate the interface force correction. The force correction procedure relies on nonlinear subiterations, as we iterate between fluid and structural equations of the fully partitioned system. The subiterations are done by cyclic substitutions within the same time step for the implicit integration operator. The iterative sequence transformation of the NIFC scheme are described in Algorithm 1. To avoid severe overshoots and undershoots, the limiter on the solutions of β can be employed at each interface degree-of-freedom I . As can be easily seen, the implementation of the NIFC correction is straightforward in a strongly coupled fluid–structure solver. With respect to the Aitken's iterated process, the difference lies in the fact that the dynamic parameter used here is automatically computed as an auxiliary sequence to stabilize the interface force during strong added mass effects.

Throughout this study, the incremental velocity and pressure are computed via the matrix-free implementation of the restarted Generalized Minimal RESidual (GMRES) solver proposed in [56]. The GMRES uses a Krylov space of 30 orthonormal vectors to solve a fully coupled pressure/velocity matrix system. In the current formulation, we perform Newton–Raphson type iterations to minimize the linearization error per time step. The solver employs a hybrid parallelism for the solution of partitioned fluid–structure solver through the stabilized finite element method. In nutshell, the parallelization relies on a standard master–slave strategy for distributed memory clusters via MPI with a domain decomposition strategy [57,58]. The master process reads the mesh and performs the partition of the mesh into subgrids using METIS (an automatic graph partitioner) [59]. Each process performs the computation for a subgrid and the remaining subgrids behave as the slaves. The slave processes form the local element matrices and the local right-hand vectors and solve the resulting system solution in parallel. The hybrid approach (mixed mode) allows to take the advantage of thread-level parallelism of multicore architecture and also to enable one MPI task accessing all the memory of a node [60].

Algorithm 1 Nonlinear interface force correction procedure

Loop over time steps, $n = 0, 1, \dots$
 Predict displacement through extrapolation (17)
 Loop over the nonlinear iterations, $k = 0, 1, \dots, nIters$
 Solve uncoupled structure, ALE and fluid problems through a staggered cycle
 Evaluate new set of interface force component at each iteration \mathbf{f}_I^k
 (a) Initialize saved auxiliary variables $\mathbf{p} = \mathbf{1}$, $\mathbf{q} = \mathbf{0}$, and $\mathbf{r} = \mathbf{0}$
 (b) Compute values for subiteration $k > 1$
 $\alpha = p^{k-1}$
 $\delta = \mathbf{f}_I^{k-1} - \mathbf{r}^{k-1}$
 $\beta = \mathbf{q}^{k-1} - \alpha\delta$
 $\gamma = \|\mathbf{q}^{k-1}\|/\beta$ (limit β increments)
 $\mathbf{p}^k = \alpha\gamma$
 (c) Update the values:
 $\mathbf{q}^k = \mathbf{p}^k(\mathbf{f}_I^{k-1} - \mathbf{r}^{k-1})$
 $\mathbf{r}^k = \mathbf{r}^{k-1} + \mathbf{q}^k$
 $\mathbf{f}_I^k = \mathbf{r}^k$
 (d) Transfer corrected force component \mathbf{f}_I^k to solid nodes
 (e) If $|\mathbf{f}_I^k - \mathbf{f}_I^{k-1}| < \epsilon$, go to next time step

5. Numerical convergence and verification

To assess the convergence and performance of the NIFC procedure, we simulate two problems: the first numerical test verifies the second-order temporal accuracy. The second test provides a comparative assessment of NIFC with available reference data.

The vortex-induced vibration of a cylinder is strongly influenced by four key non-dimensional parameters [3], namely mass-ratio (m^*), Reynolds number (Re), reduced velocity (U_r), and damping ratio (ζ) defined as:

$$m^* = \frac{M}{m_f}, \quad Re = \frac{\rho^f U D}{\mu^f}, \quad U_r = \frac{U}{f_N D}, \quad \zeta = \frac{C}{2\sqrt{KM}}, \quad (44)$$

where M is the mass per unit length of the body, C and K are the damping and stiffness coefficients, respectively for an equivalent spring–mass–damper system of a vibrating structure, U and D the free-stream speed and the diameter of cylinder, respectively. The natural frequency of the body is given by $f_N = (1/2\pi)\sqrt{K/M}$ and the mass of displaced fluid by the structure are $m_f = \rho^f \pi (D^2/4)L_c$ and $m_f = \rho^f D^2 L_c$ for circular and square cross-sections, respectively, and L_c denotes the span of the cylinder. In the above definitions, we assume that the translational motion of the rigid body is isotropic, i.e., the mass vector $\mathbf{m} = (m_x, m_y)$ with $m_x = m_y = M$, the damping vector $\mathbf{c} = (c_x, c_y)$ with $c_x = c_y = C$, and the stiffness vector $\mathbf{k} = (k_x, k_y)$ with $k_x = k_y = K$. The fluid loading is computed by integrating the surface traction considering the first layer of elements located on the cylinder surface. The instantaneous force coefficients are defined as

$$C_L = \frac{1}{\frac{1}{2}\rho^f U^2 D} \int_{\Gamma} (\boldsymbol{\sigma}^f \cdot \mathbf{n}) \cdot \mathbf{n}_y d\Gamma, \quad (45)$$

$$C_D = \frac{1}{\frac{1}{2}\rho^f U^2 D} \int_{\Gamma} (\boldsymbol{\sigma}^f \cdot \mathbf{n}) \cdot \mathbf{n}_x d\Gamma. \quad (46)$$

Here \mathbf{n}_x and \mathbf{n}_y are the Cartesian components of the unit normal, \mathbf{n} . In the present study, C_D and lift coefficient C_L are postprocessed using the conservative flux extraction of nodal tractions along the fluid–body interface. As shown in [61], the conservative flux approach provides much more accurate approximation than the direct evaluation of interface fluxes. Further details regarding the traction flux evaluation can also be found in [62–64].

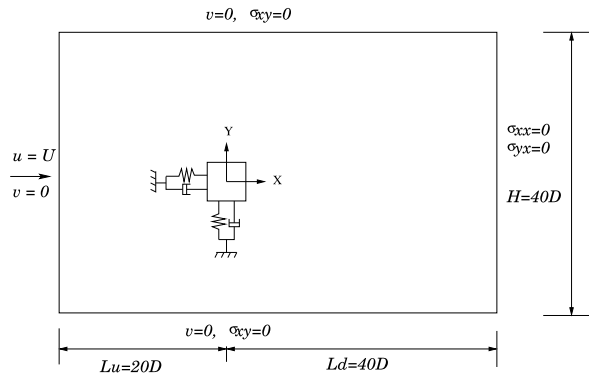


Fig. 1. Schematic diagram of the domain used for simulating flow around a square cylinder at zero incidence.

Table 1

Grid convergence study with parameters $Re = 100$, $m^* = 3$ and $U_r = 5$.

Parameter	M1	M2	M3	M4
No. of nodes	17,622	34,302	71,552	145,608
No. of elements	17,389	34,027	71,199	145,195
Time-step size Δt	0.01	0.01	0.01	0.01
Average frequency \bar{f}	0.1633	0.1633	0.1633	0.1633
Average amplitude \bar{A}/L	0.0974 (55.94%)	0.1996 (9.72%)	0.2195 (0.72%)	0.2211
Average drag coeff. \bar{C}_d	1.6231 (24.07%)	1.9941 (6.71%)	2.1338 (0.18%)	2.1377
Lift coeff. rms C_l^{rms}	0.4845 (29.71%)	0.6042 (12.35%)	0.6872 (0.30%)	0.6893

5.1. Convergence study

The VIV of a square cylinder at $Re = 100$, $m^* = 3$ and $\zeta = 0$ is considered for the convergence study of the NIFC scheme. Fig. 1 illustrates a schematic of the two-dimensional simulation domain used in the convergence study. The center of the square column is located at the origin of the Cartesian coordinate system. The side length of square column is unity and noted as D . The distances to upstream and downstream boundaries are $20D$ and $40D$, respectively. The distance between side-walls is $40D$, which corresponds to blockage of 2.5%. The square column is free to oscillate in in-line (streamwise) and transverse directions. The flow velocity U is set to unity at the inlet and no-slip or wall function is implemented at the surface of square column. The top and bottom boundaries are defined as slip walls.

5.1.1. Grid convergence

The domain is discretized using an unstructured finite-element mesh. The grid, noted as $M1$, comprises of 17 389 elements. There is a boundary layer mesh surrounding the square column and triangular mesh outside the boundary layer region. Each side of the square column is discretized with 40 uniformly distributed nodes. The first layer of the boundary layer mesh is placed at $0.01D$ from the column wall. Besides, the central area surrounding the square column contains 9644 elements. Three more grids are generated where the mesh elements are successively increased by a factor of 2. They are designated as $M2$, $M3$ and $M4$, respectively. The discretized domain, along with a magnified view of the corners of square column is shown in Fig. 2. All cases are run at $Re = 100$, $m = 3$ and $U_r = 5$. Results of the grid convergence study are recorded in Table 1 for the lock-in region. Table 2 summarizes the grid convergence results at $U_r = 3$, which is away from the lock-in region. A good convergence can be observed between $M1$ and $M2$. Since a closed-form exact solution for this physical problem is not available for the lock-in at $U_r = 5$, the numerical solutions corresponding to the finest grid $M4$ have been considered as the reference values. The values within the bracket denote the percentage difference in numerical solutions with respect to the mesh $M4$. It can be seen that the relative error values recorded for mesh $M3$ and $M4$ differ by less than 1%. Therefore, the mesh $M3$ is selected to proceed with the time-step convergence study.

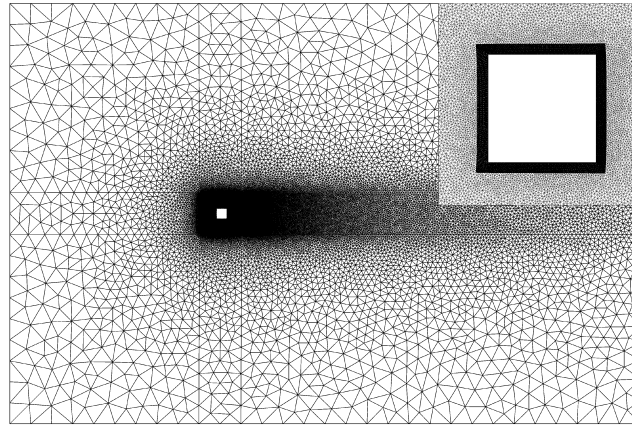


Fig. 2. Representative finite element mesh (*M1*) used for convergence study.

Table 2

Grid convergence study with parameters $Re = 100$, $m^* = 3$ and $U_r = 3$.

Parameter	<i>M1</i>	<i>M2</i>
No. of nodes	17,622	34,302
No. of elements	17,389	34,027
Time-step size Δt	0.01	0.01
Average frequency \bar{f}	0.1367	0.1367
Average amplitude \bar{A}/L	0.0104 (0.95%)	0.0105
Average drag coeff. \bar{C}_d	1.5696 (0.50%)	1.5775
Lift coeff. rms C_l^{rms}	0.3016 (0.81%)	0.2992

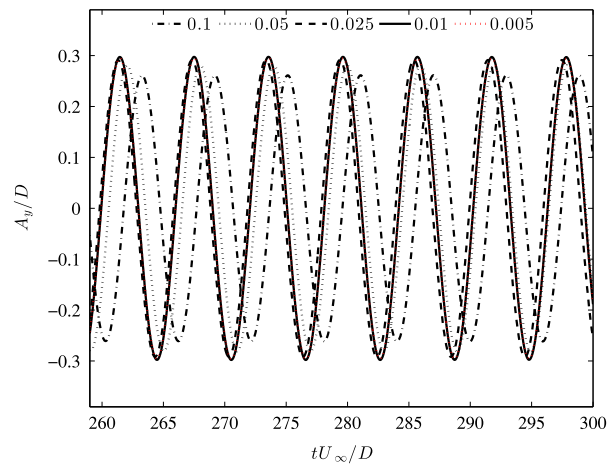


Fig. 3. Temporal convergence study: Dependence of transverse amplitude on time-step size for a freely vibrating square cylinder.

5.1.2. Time-step convergence

To perform a temporal convergence study, cases are run at constant time-steps of $\Delta t = 0.1$, 0.05 , 0.025 and 0.01 . Fig. 3 shows the time histories of transverse displacement of the square column recorded for each case. Since a closed-form exact solution for this physical problem is not available, we consider the values obtained at $\Delta t = 0.005$ as a reference value for the error analysis. Transverse amplitudes of the structure obtained at $\Delta t = 0.01$ and $\Delta t = 0.005$ are within 1% of each other. To achieve stationary vibrational response, the time step of $\Delta t = 0.01$ is selected for the simulations in the study presented hereafter.

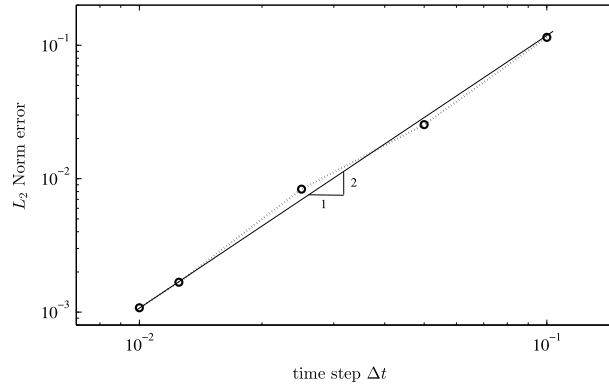


Fig. 4. Second order temporal convergence of the NIFC procedure.

Fig. 4 shows the error for the amplitude in standard discrete least-square norm L^2 . From the figure, it is evident that the line plotted has a slope of $m = 2$, which clearly confirms the second-order accuracy of the NIFC scheme. Through the Taylor series arguments and the partial sum of eigenvector sequence, a brief proof of the second-order convergence of the interface force extrapolation is provided in [Appendix B](#).

5.2. Response characteristics and verification

To assess the response characteristics, we continue with the freely vibrating square cylinder at $Re = 100$, $m^* = 3$ and $\zeta = 0$. Fig. 5(a) shows the time history of vibrating amplitudes at $U_r = 4.95$. As expected, the amplitude of in-line vibration is much smaller than those in the transverse direction. When the flow reaches the equilibrium state after nondimensional time $t = 200$, the beating pattern can be observed in the displacement response. The transverse amplitude A_y/D varies from 0.28 to 0.31 which is different from those out of the lock-in region which displays a regular and constant amplitude with a single frequency. The beating pattern can be further seen in Fig. 5(b) through the time history of drag and lift coefficients.

To validate the present numerical model, the case of flow past a 2-DOF square cylinder at $Re = 100$, $m^* = 3$ and $U_r \in [1, 20]$ is simulated and compared with the data from [65]. The cross-flow vibration amplitude A_y/D is defined as $A_y = (Y_{\max} - Y_{\min})/2D$, where Y_{\max} and Y_{\min} denote the maximum and minimum displacements of the vibrating cylinder in Y -direction, respectively. Fig. 6(a) shows the variations of the vibration amplitude A_y/D with respect to the reduced velocity. The range of $U_r < 4$ represents the pre-lock-in regime, where vibration amplitudes are negligibly small. As U_r increases, the vortex shedding frequencies (and thus the periodic force frequencies) synchronizes with the vibration frequencies, and the lock-in range is entered. In the initial branch, the vibration amplitudes increase as U_r is increased before reaching a peak. The difference of A_y between the two studies is within 1% for all the reduced velocities. In the lock-in region from $U_r = 4$ to $U_r = 6$, the variation of A_y is quite sensitive to the change of U_r , therefore, five more cases are simulated at $U_r = 4.6, 4.7, 4.8, 4.9$ and 4.95 . Fig. 6(b) shows the XY trajectories of the freely vibrating cylinder. As found in [65], the trajectories are in the shape of skewed figure-8, whereby the magnitude of the in-line direction X is much smaller than that in the cross-flow direction Y . Fig. 7 shows the vorticity contours at $U_r = 5$ and 6 in the lock-in regime at the instants when the cylinder is at the mid and peak (minimum) locations. At $U_r = 5$, the shed vortices form a double-row like configuration for both the instants. On the other hand, two single (2S) vortices are found to be shed from the cylinder at $U_r = 6$ whereby the vibration amplitude is very small.

6. Investigation of mass ratio effects

In this section, we investigate the effects of low mass ratio on the stability of NIFC and strong staggered coupling (SSC) schemes based on the block-iterative Newton method [12]. In particular, we would like to investigate the effectiveness of the NIFC transformation with respect to the untransformed iterative sequence corresponding to the SSC method. Mass ratio is a representative of the inertia effects in a fluid–structure problem. For the lower mass ratios, the physics of the problem is dominated by the inertia effects of the fluid, whereas higher mass ratios correspond to problems in which the structural inertia effects are dominant. The VIV of a circular cylinder is simulated at wide

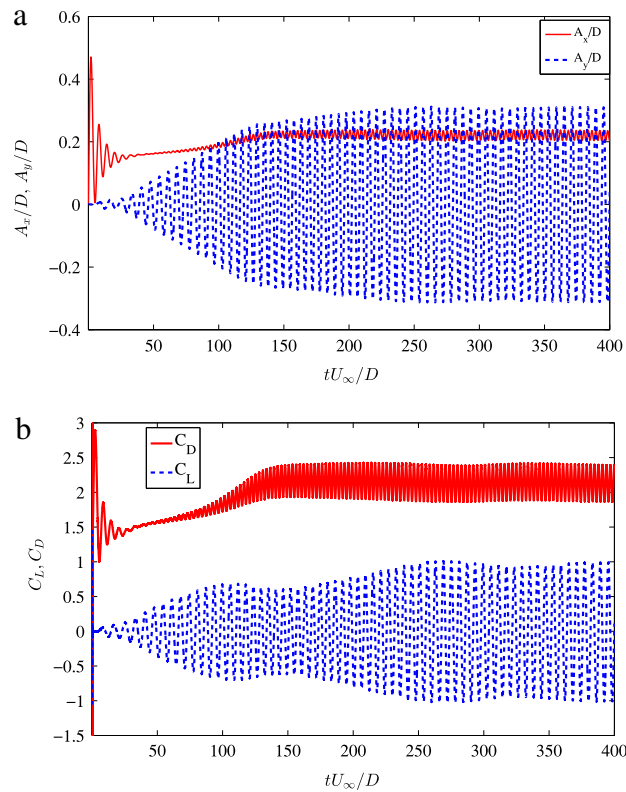


Fig. 5. Representative results of freely vibrating square cylinder at $U_r = 5.0$: (a) vibration amplitude (b) force coefficients.

range of mass ratios to assess the robustness of the two schemes. Similar to the square cylinder, the unstructured mesh around the circular cylinder is shown in Fig. 8.

6.1. Transverse oscillations of circular cylinder at high mass ratio $m^* = 10$

To compare the two coupling strategies, the case of a circular cylinder oscillating in the (x, y) plane was considered. The Reynolds number was set to $Re = 100$, the reduced velocity was $U_r = 5.0$, and the damping ratio was 0.0. The computational domain and boundary condition set-up is similar to the one used for the oscillating square cylinder.

We first consider the case of $m^* = 10.0$. Both the SSC and NIFC schemes are equally stable for this mass ratio, and approached similar periodic steady-states. Fig. 9 shows a good comparison of staggered strong coupling (SSC) and NIFC schemes at $m^* = 10.0$. The force coefficients and response characteristics are within 0.5%.

6.2. X–Y vibrations of circular cylinder at low mass ratio $0.25 \leq m^* \leq 1.0$

Fig. 10 shows the effects of mass ratio on the stability of SSC and NIFC schemes for $0.52 \leq m^* \leq 0.75$. The step-to-step oscillations can be observed in the SSC scheme. For $m^* = 0.52$, the SSC scheme completely fails even for 5 nonlinear iterations between fluid and rigid-body dynamics. The SSC, on the other hand, becomes unstable soon after the computation is initialized. Fig. 10 shows the large oscillations of the center of the cylinder that eventually leads to an exponential instability. However, the proposed NIFC scheme provides a stable solution, even for such a low mass ratio for incompressible fluid interacting with vibrating structure at resonance condition.

The NIFC corrections provide sufficient control to contain the coupled instabilities beyond the critical mass ratio observed for the standard strong coupling (SSC) and standard Aitken's extrapolation (SAE) scheme without α -stabilization. Fig. 11 shows the comparison of force residual updates with respect to the iterations in a single time step for the NIFC procedure, the standard subiteration (SSC) and the Aitken's extrapolation without α -stabilization. The SSC procedure provides non-decaying force update for both mass ratios $m^* = 0.52$ and $m^* = 0.26$. The standard

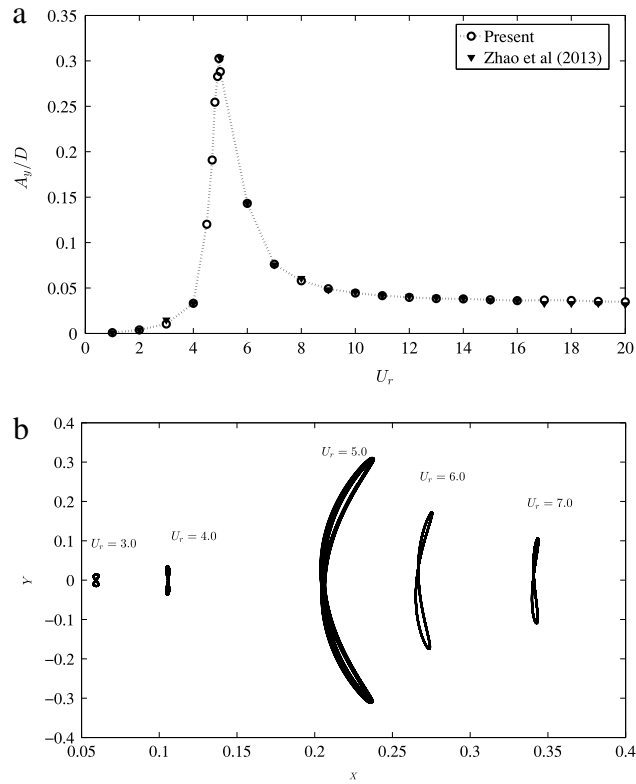


Fig. 6. VIV results of freely vibrating square cylinder at reduced velocity $U_r = 5$: (a) vibration amplitude, (b) XY trajectories.

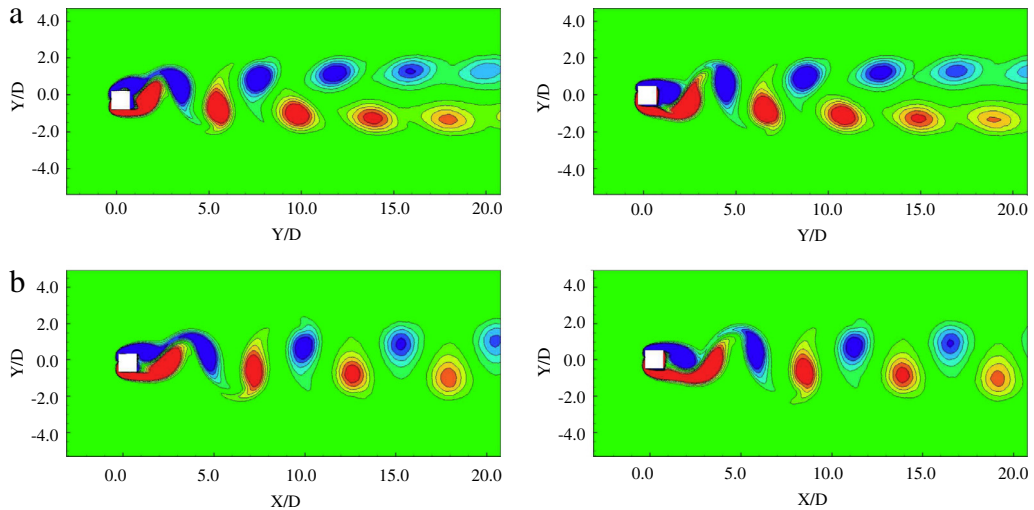


Fig. 7. Instantaneous vorticity contours for square-cylinder at minimum-position (left) and at mid-position (right): (a) $U_r = 5$ (b) $U_r = 6$.

Aitken's extrapolation provides a convergent force update for $m^* = 0.52$, but it suffers with a non-convergent force update for $m^* = 0.26$. On the other hand, the NIFC procedure performs consistently for both the mass ratios. The vorticity contours for the case of maximum amplitude in the lock-in regime ($Re = 100$, $U_r = 5.0$) are shown in Fig. 12. The expected 2S mode pattern (two single vortices per cycle of motion) can be seen in the wake, which is in agreement with the observations of [66].

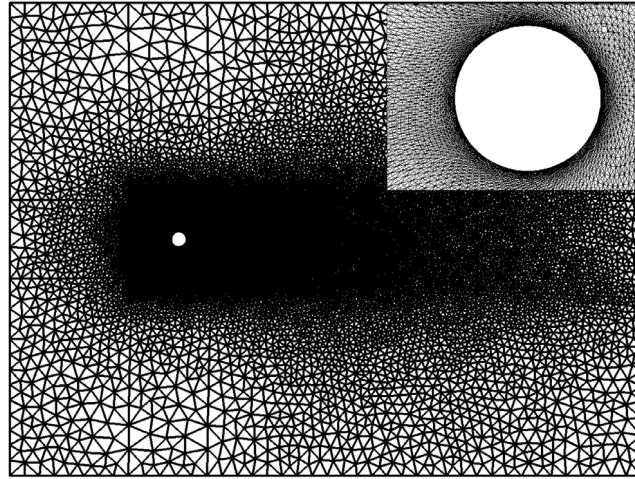


Fig. 8. Cylinder VIV problem with full computational mesh with close-up deformed unstructured mesh around the body (right top corner).

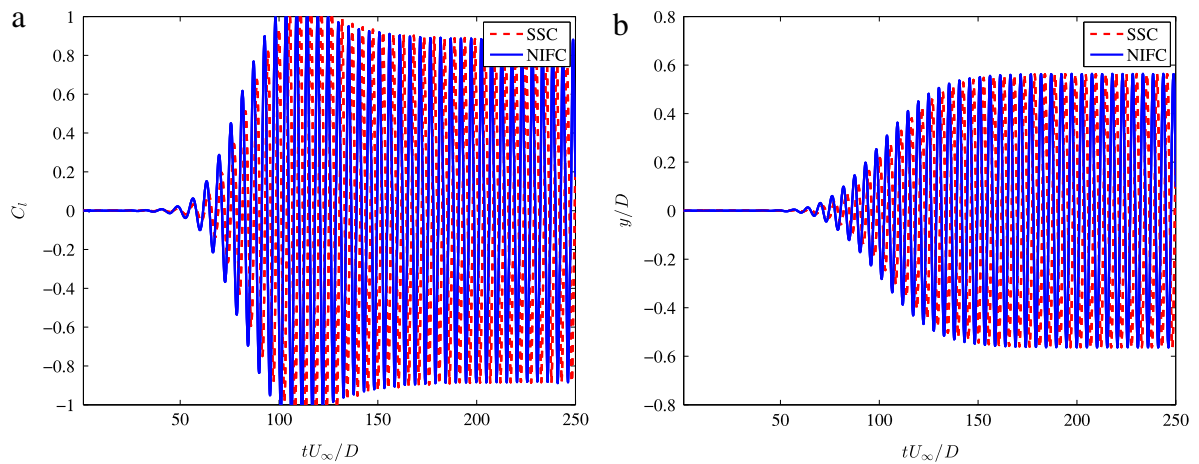


Fig. 9. Comparison of transverse responses of SSC and NIFC at $m^* = 10.0$, $Re = 100$ and $U_r = 5$: (a) lift force, (b) transverse amplitude. Both schemes utilize 4 nonlinear iterations per time step.

Fig. 13 shows the inherent instability in the strong staggered scheme due to the strong nature of fluid–structure coupling. For incompressible fluid interacting with low mass structures, reducing the time step size does not cure the instability regardless of whether the Courant condition for the individual domain is satisfied, which is consistent with the findings of [17,19]. The strong coupling with several non-linear iterations attempts to minimize the coupling errors during a time step. However, at critical low mass ratio, eventually the coupled instabilities in the fluid–structure system lead to a complete blow-up of the SSC procedure and the iterated interface force sequence diverges quite strongly due to the complexity of the computations associated with added mass effects [19,24]. In the case of vortex-induced vibrations, small errors in displacement predictions would lead to large errors in the computations of transverse force. The NIFC scheme provides iterative force corrections with the aid of stabilization sequence when the brute-force subiterations perform poorly and lead to severe numerical instabilities for low-mass structures subjected to strong added-mass effects.

7. Application of vibrating tandem square cylinder

Square shaped columns are widely used in semi-submersibles and offshore floating structures. Predicting flow-induced vibrations in multi-column floaters is a challenging task due to complex wake interference and galloping, a self-excited non-linear instabilities associated with large amplitude oscillations and is undesirable to avoid structural

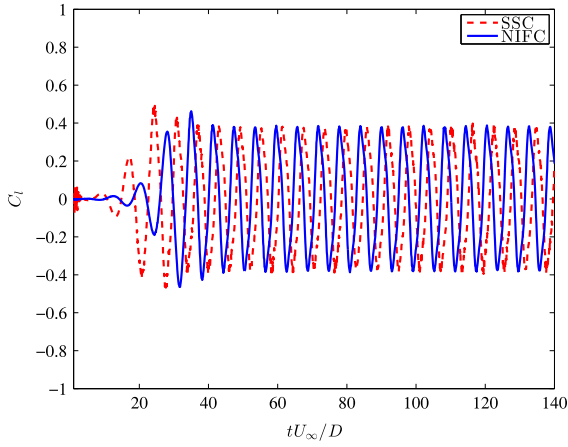
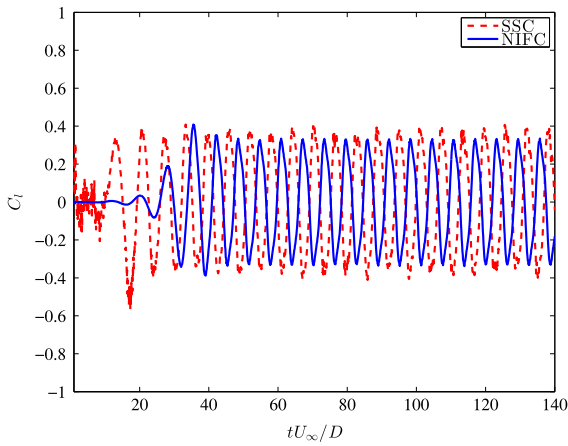
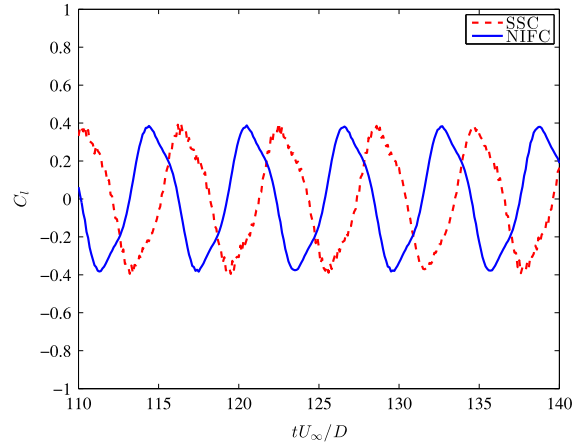
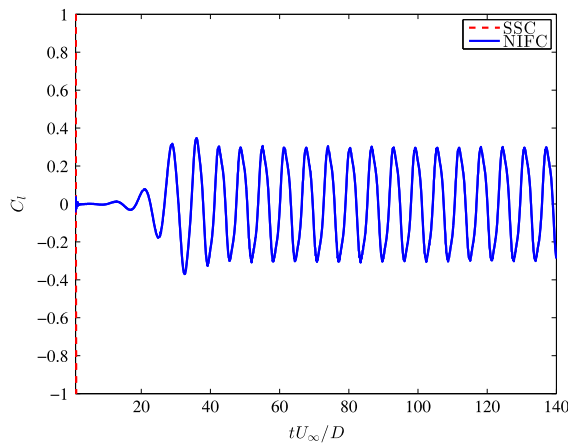
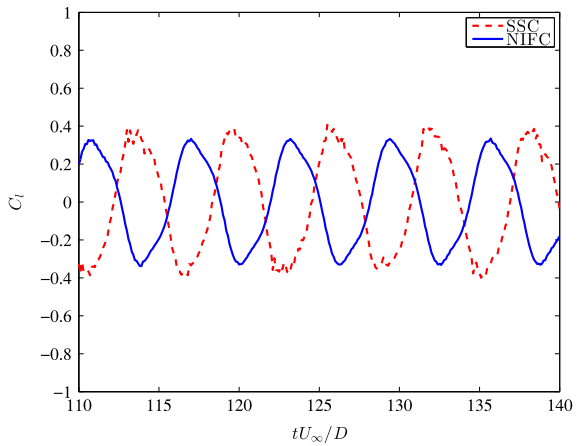
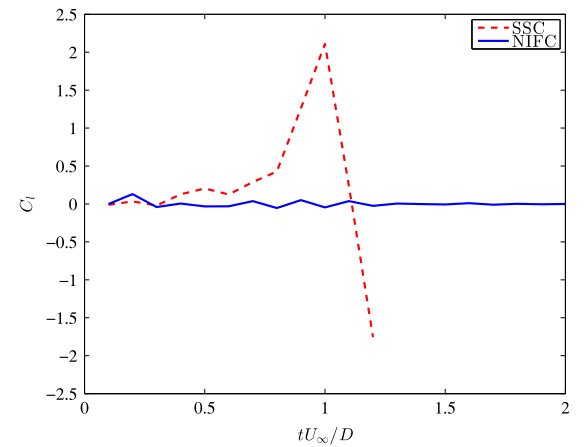
(a) Mass ratio $m^* = 0.75$.(b) Mass ratio $m^* = 0.6$.(c) Mass ratio $m^* = 0.52$.

Fig. 10. Effects of mass ratio on the stability of strong staggered coupling (SSC) and nonlinear interface force correction (NIFC) at $Re = 100$ and $U_r = 5$. Both schemes utilize 4 nonlinear iterations per time step.

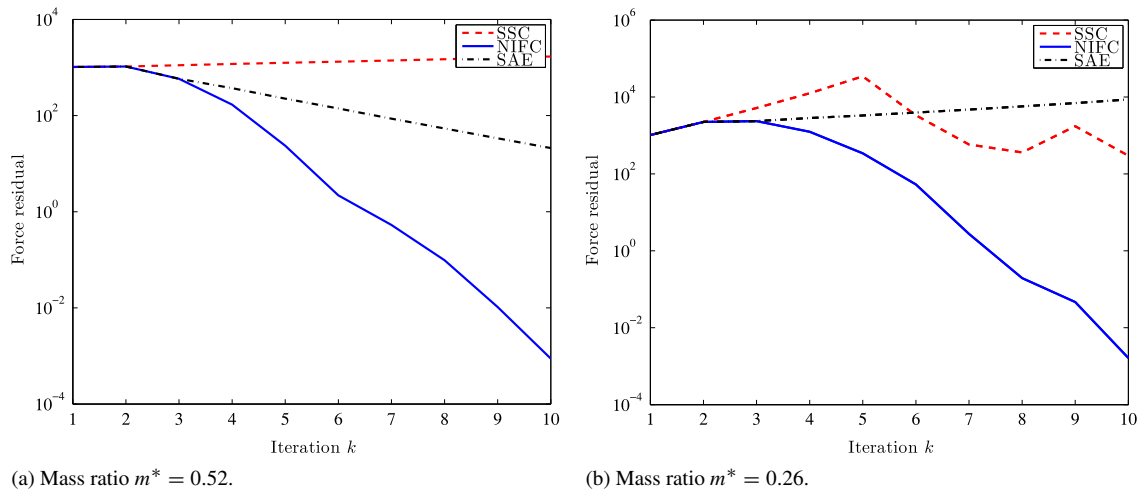


Fig. 11. Comparison of the force residual update for the nonlinear iterative force correction (NIFC), strong staggered coupling (SSC) and standard Aitken's extrapolation (SAE) without α -stabilization.

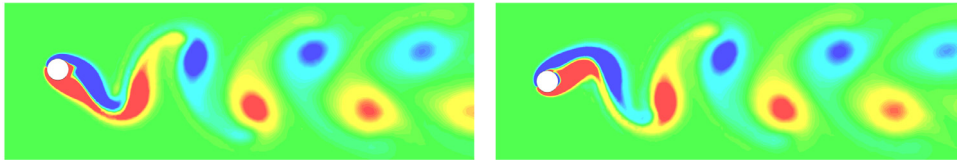


Fig. 12. Freely vibrating cylinder in the cross-stream direction: Instantaneous spanwise vorticity isolines for case $Re = 100$, $m^* = 0.5$ and $U_r = 5.0$ with non-dimensional time interval of $tU/D = 2.0$.

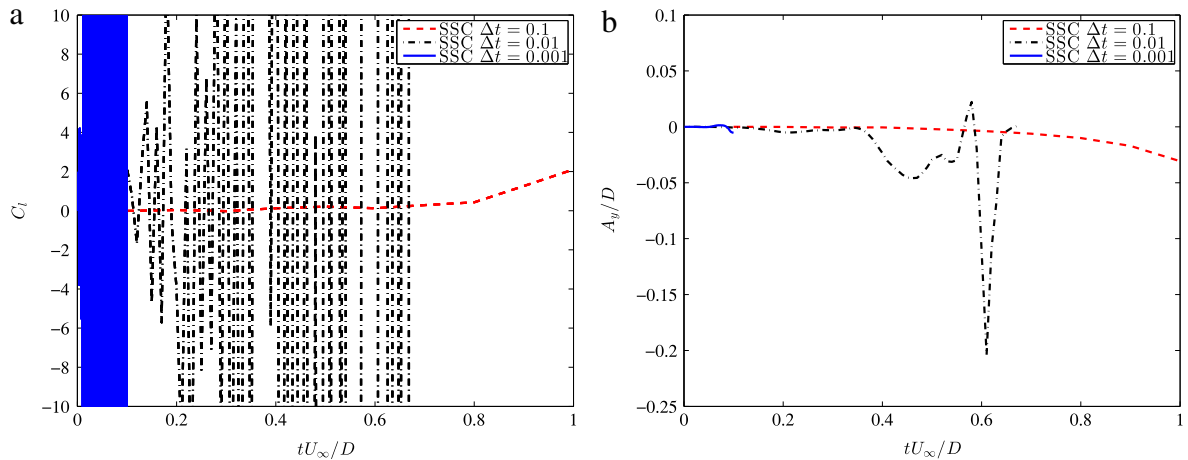


Fig. 13. Dependence of strong staggered coupling (SSC) on time-step size Δt at $m^* = 0.5$, $Re = 100$ and $U_r = 5$: (a) transverse force, (b) amplitude.

failure. This section reports a set of numerical experiments to understand flow-induced vibrations of the square columns kept in a tandem arrangement. Results on the coupled force and response dynamics are presented for an isolated column and for a pair of square columns in the tandem configuration where downstream column is elastically mounted and free to oscillate in in-line and transverse directions. We assess the combined wake-induced and sharp-corner based galloping effects on the downstream column by comparing with the isolated square column counterpart. It is known that the circular cylinders undergo vortex-induced motion alone whereas motion of a square column

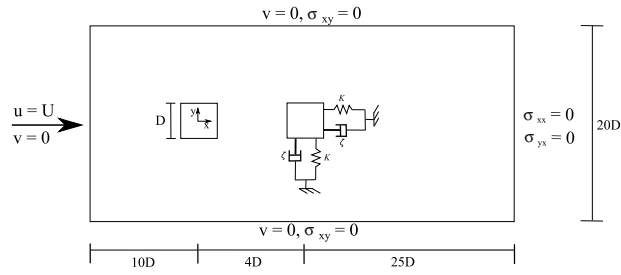


Fig. 14. Schematic diagram of the geometric arrangement and boundary conditions for tandem square column cases.

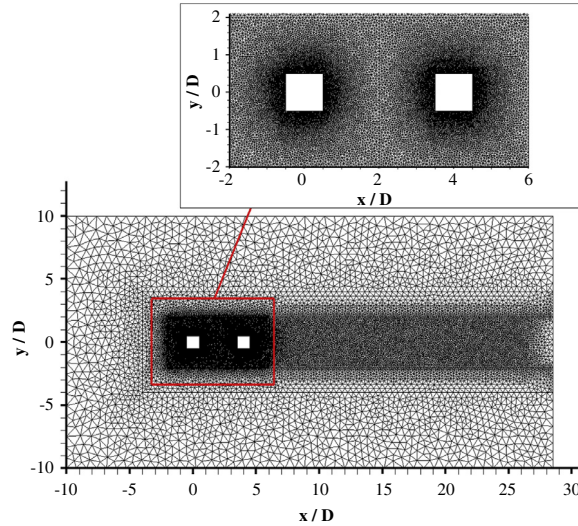


Fig. 15. Unstructured finite element mesh for tandem square cylinder configuration.

is vortex-induced at low Re and galloping at high Re [67,68]. The effects of reduced velocity on the fluid forces, amplitudes, wake contours, and the phase angles will be analyzed.

The two-dimensional simulation domain illustrated in Fig. 14 describes a set-up with two square columns kept in tandem arrangement. All the dimensions are normalized with the side length of the column, denoted as D . The columns are separated by a center-to-center distance of $4D$. The downstream column has two degrees-of-freedom. The inlet boundary is placed at a distance of $10D$ from the upstream column and outlet is placed at a distance of $25D$ from the downstream column. The top and bottom boundaries are defined as slip walls. Discretization is carried on the basis of the outcome from grid independence study for the single square cylinder. A triangular finite element mesh was generated comprising a total of 104 650 elements as shown in Fig. 15. Reasonable resolutions of the boundary layers and the wakes of upstream and downstream columns. Region near to the structural members is discretized with approximately 20 nodes in the normal direction to the wall and the nodes are placed as close as $0.02D$ in the normal direction from wall.

Simulations are conducted for the range $2 \leq U_r \leq 40$ with an objective to examine the response of downstream column in the initial, lock-in as well as galloping branches. The mass ratio and Reynolds number were kept constant at $m^* = 5$ and $Re = 200$, respectively. The damping ratio was kept zero in order to realize maximum amplitudes during oscillations.

7.1. Response characteristics

From the displacement trajectories shown in Fig. 17, for the downstream column, we notice that the amplitudes of transverse oscillation are substantially higher than the in-line oscillations. The column traces a characteristic “8” shape in the initial branch and skewed elliptical trajectory at the higher U_r values. With the onset of galloping the trajectory

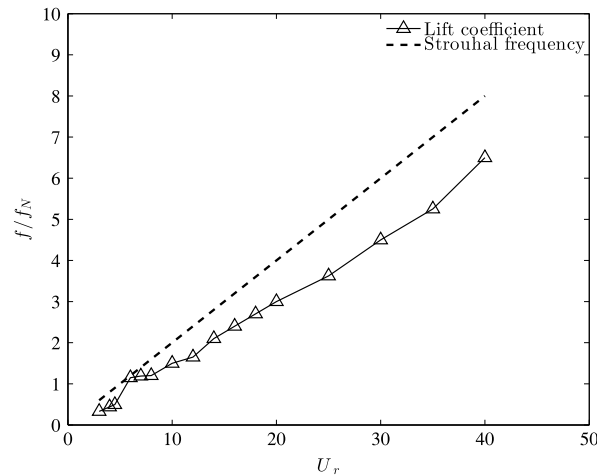


Fig. 16. Frequency of the lift forces acting on the tandem downstream square cylinder.

develops into an open loop. This particular sequence of changes in the column trajectory is unique when compared with trajectories of an isolated square column reported by [65]. The frequency of oscillation of the downstream column is plotted against U_r in Fig. 16. The results demonstrate a well defined lock-in region for $6 \leq U_r \leq 8$ where the oscillation frequency closely matches the natural frequency of the structure. However, the onset of lock-in window has shifted towards higher reduced velocities when compared to the response of isolated square column in a uniform flow [65].

Fig. 18 shows the time histories of lift coefficient and transverse displacement of the downstream column at representative U_r values. Except in the lock-in branch, both signals exhibit a sinusoidal behavior everywhere. In the initial regime, lift force oscillations are in-phase with displacement oscillations, whereas in the galloping (quasi-periodic) regime the signals are out of phase, which is illustrated in Fig. 19. In the lock-in regime, the lift coefficient signal leads the displacement signal by a small angle. The force signal also possesses components at frequencies other than that of displacement signal.

Fig. 20 illustrates the variation of drag forces on the downstream column along with the corresponding in-line motions. The column experiences negative drag in the initial regime and therefore gets sucked into the wake of the upstream column. In the lock-in and the galloping regimes, the downstream column experiences a positive drag and therefore gets pushed back.

Fig. 21 shows the root mean square values of the transverse displacement experienced by the downstream column plotted against corresponding reduced velocities U_r . The results from the isolated square cylinder are also included for comparison. For the tandem square cylinder, the components of response are the initial and lower branches of VIV, desynchronization and galloping [10]. The maximum displacement amplitude is found for the tandem arrangement at $U_r = 10$. It is nearly 1.5 times the maximum displacement of the single square column which appears at $U_r = 5$. For the single column set-up, the displacement amplitude is largest in the range $4 \leq U_r \leq 7$. For $U_r \geq 7$, the transverse response y^{rms} suddenly drops and remains nearly constant for $U_r \geq 10$. For the tandem arrangement, the displacement amplitude increases up to $U_r = 10$, with small dip in the lock-in region, and decreases gradually as the U_r increases up to 15. For $U_r \geq 15$, the displacement amplitude remains constant at a value nearly five times higher than that of a single column arrangement.

7.2. Vortex organization

The wake of the upstream cylinder interacts with the boundary layer of the downstream cylinder, which influences the flow contours on the downstream cylinder. Due to the wake interaction the pressure on the low suction side is reduced on the downstream cylinder, increasing the lift and in-turn the response. Fig. 22(a) through 22(f) illustrate the vorticity contours at selected reduced velocities. The contour plots suggest that in the initial regime the downstream column oscillates within the wake of the upstream column. As shown in Fig. 22(a), the shear layer separated from the upstream column effectively encapsulates downstream column and there is no individual vortex shedding from the

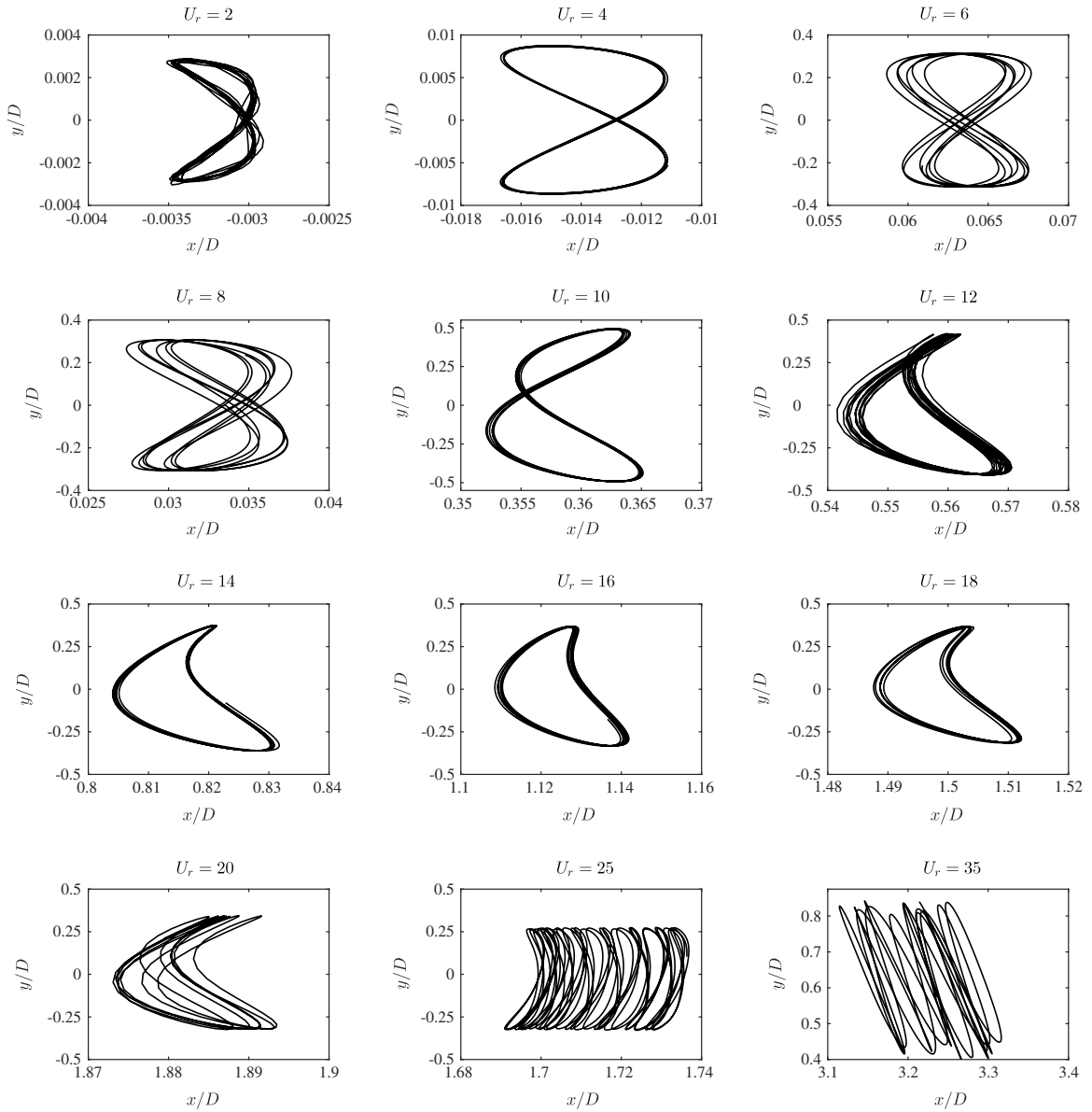


Fig. 17. Displacement trajectories of the tandem downstream square cylinder.

columns. The lock-in and galloping regimes are characterized by positive drag on the downstream column resulting in an increase in center-to-center spacing and augmented transverse oscillations. Consequently, the extended shear layer destabilizes leading to the commencement of individual vortex shedding from the columns. The vortex shedding is occurring in a 2S mode in the lock-in regime which further transforms to a 2P-like mode in the desynchronization regime. In the galloping regime, the wake structures are somewhat wide and irregular and the phase angle is consistently close to 180° with the trajectories of skewed elliptical shapes. A detailed investigation of the vortex dynamics and wake topology is beyond the scope of this study.

8. Conclusions

To overcome the deficiencies in partitioned schemes for FSI, we have developed a subiteration based nonlinear iterative force correction procedure for fluid–body interactions. The new procedure relies on the iterative transformation of the interface force sequence with the aid of generalized Aitken’s iterated Δ^2 process and a dynamic

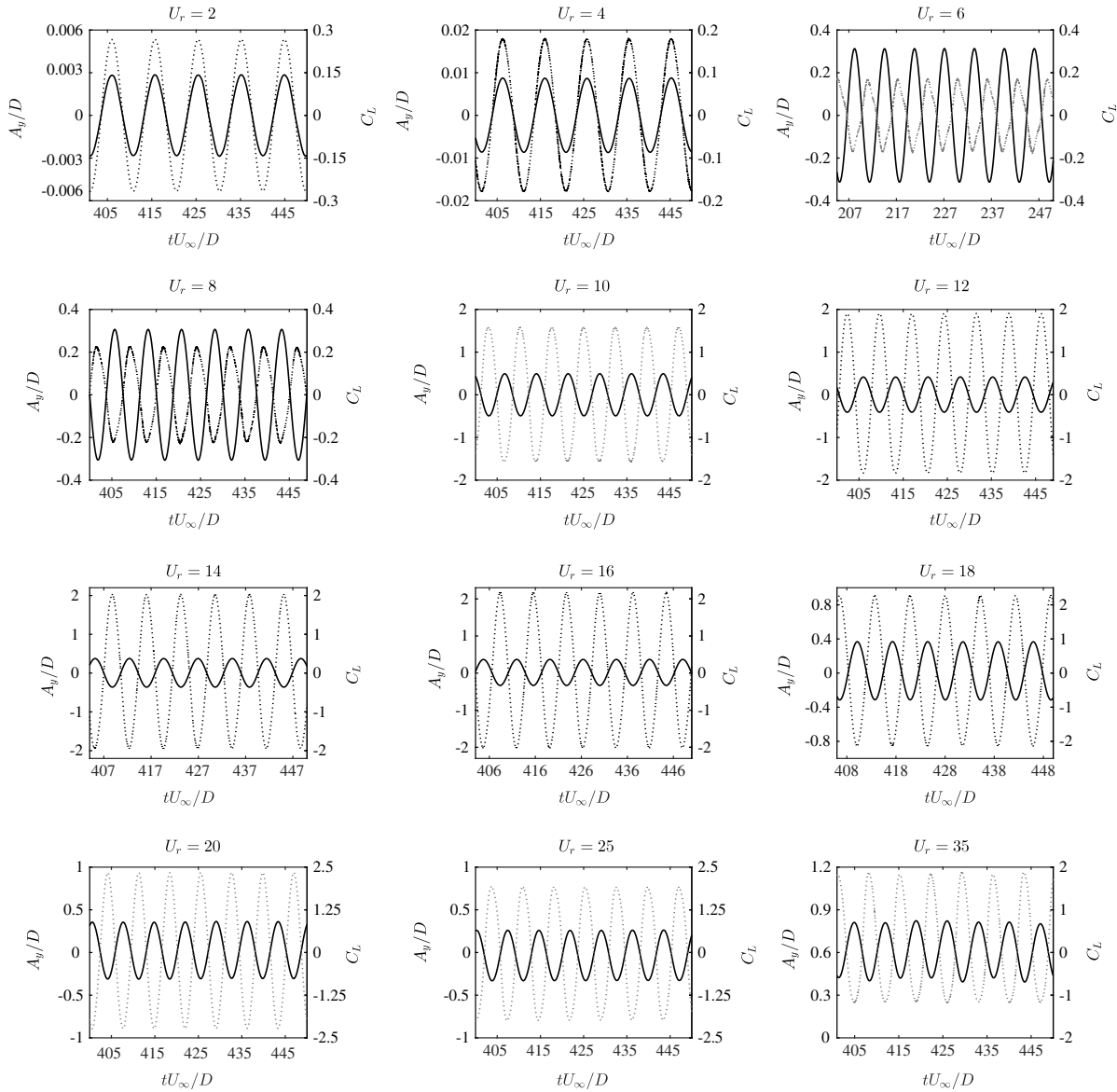


Fig. 18. Time histories of the transverse displacement (solid lines) and lift coefficients (dash lines) of the downstream column at selected values of U_r .

stabilization parameter. The interface force sequence transformation can be easily implemented in existing strongly coupled FSI solvers, while retaining the modularity of both codes. The coupled solver is validated against the published vortex-induced vibration results of flow past a square cylinder. The NIFC algorithm produces satisfactory results which are consistently equal or superior to those produced by a strongly coupled scheme based on fixed-point subiteration for the mass-ratio range of $0.25 \leq m^* \leq 10$ and there is no tunable stability parameter. Second-order temporal accuracy of the NIFC scheme has been confirmed through a systematic convergence analysis. Through the VIV of circular cylinder, we demonstrate that the NIFC scheme equipped with the dynamic stabilization parameter is essential to the simulations of low mass ratio vortex-induced motion problems, in which strong coupling schemes based on subiteration may fail. Two-dimensional incompressible flow past a freely vibrating square column in standalone and tandem arrangements at low Reynolds number explored systematically. The influence of the reduced velocity on the response of downstream column is studied while keeping the mass ratio and Reynolds number constant. The downstream column experiences larger transverse lift force due to the wake interaction from the upstream column.

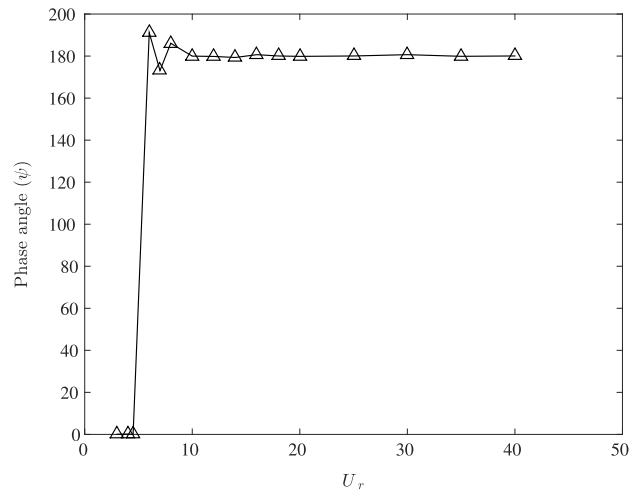


Fig. 19. Variation in phase angle between transverse displacement and lift coefficient with U_r for the downstream tandem square cylinder.

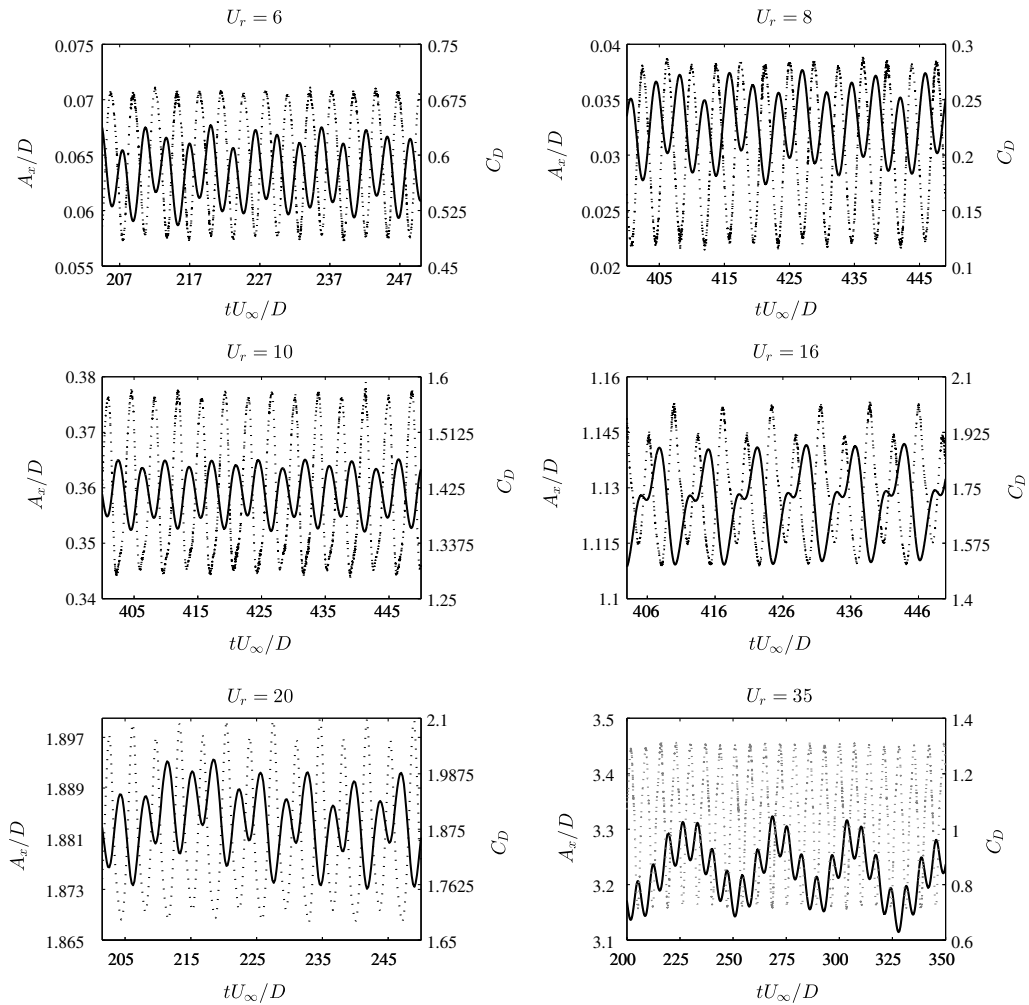


Fig. 20. Time histories of the in-line displacement (solid lines) and drag coefficients (dash lines) of the downstream cylinder at selected values of U_r .

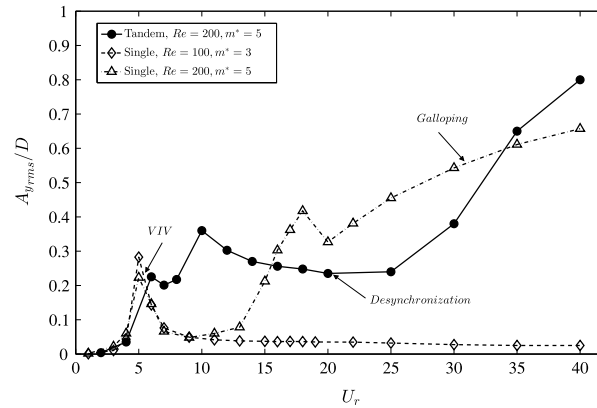


Fig. 21. Comparison between RMS values of the transverse displacements for the downstream tandem and isolated cylinder configurations at two different mass ratio and Reynolds numbers.

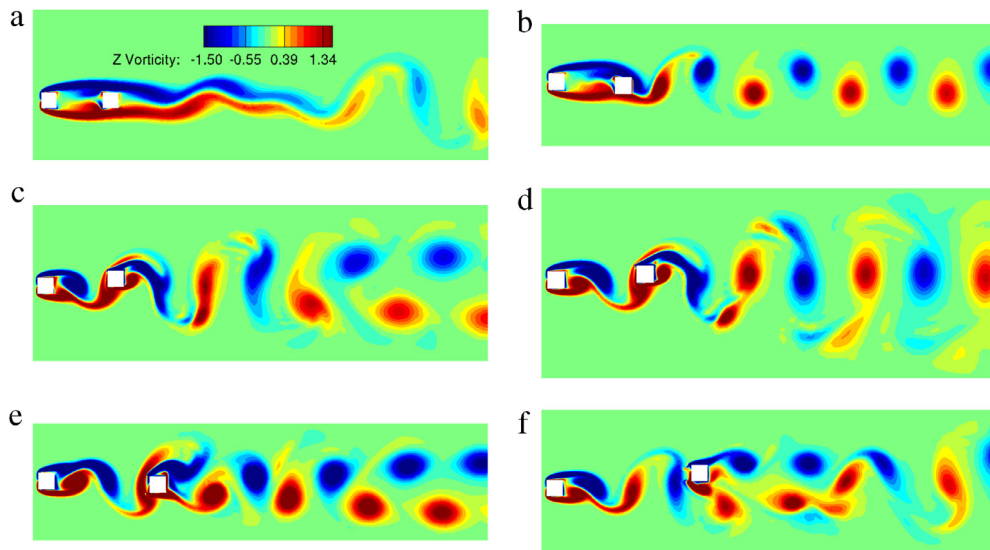


Fig. 22. Instantaneous vorticity contours for reduced velocity $U_r =$ (a) 4.5, (b) 7.0, (c) 10.0, (d) 16.0, (e) 30.0, (f) 40.0.

The oscillatory upstream wake interacting with the downstream column enforces the shedding frequency on the downstream column as the primary frequency content in the lift. Furthermore, the average displacement amplitude of the downstream column displays evident deviation from the single column arrangement due to the wake interference.

Certainly, the possibilities for modifying the basic NIFC scheme are numerous. To improve the computational efficiency of the iterative coupling scheme, we can further employ accurate and consistent prediction techniques in order to accelerate the subiteration convergence per time-step. As a low-pass filtration-like technique, the NIFC procedure is practical and generic in nature for coupled nonlinear dynamical systems to suppress overshoots (maxima) or undershoots (minima). Finally, there is a need for rigorous numerical analysis to quantify the error convergence of the nonlinear iterations for very low-mass ratios.

Acknowledgments

The first author wishes to acknowledge support from the Ministry of Education, Academic Research Fund (AcRF), Singapore with Grant number R-265-000-420-133. The second and third authors thank the National Research Foundation (R-261-507-009-281) and SMMI-Institute of High-Performance Computing (A*STAR) (R-265-000-484-305) for supporting this work, respectively. The comments of the referees were appreciated very much by the authors. The first author is deeply thankful to Dr. Shakib for many helpful discussions related to eigenvalue analysis.

Appendix A. Generalized Aitken's process for interface force

For the sake of completeness, we introduce some basic steps to derive a generalized Aitken's iterated Δ^2 process for a known sequence and with the aid of unknown parameter sequence. Let us consider a sequence of interface force component numbers $f_I = f^1, f^2, f^3, \dots, f^N$ where N denotes the interface degrees of freedom. Without loss of generality, we consider the fixed-point iteration for the solution sequence of f^1 . The kernel of computationally stable Aitken's Δ^2 process [50] is the set of sequence transformations in the following form $T : (f_k^1) \mapsto (T^{(k)})$

$$T^{(k)} = f_k^1 - \frac{(\Delta f_k^1)^2}{\Delta^2 f_k^1}, \quad k = 0, 1, \dots \quad (\text{A.1})$$

where Δ is the forward difference operator as $\Delta f_k^1 = f_{k+1}^1 - f_k^1$ and the denominator is $\Delta^2 f_k^1 = \Delta f_{k+1}^1 - \Delta f_k^1$. Next we introduce the error amplification with a dynamic update procedure and establish a connection with the standard Aitken's sequence transformation process.

At the initial iteration, we can construct the force residual Δe_1 as:

$$\Delta e_0 = f_1^1 - f_0^1 \quad (\text{A.2})$$

$$\Delta \tilde{e}_1 = \alpha_1 \Delta e_1 \quad (\text{A.3})$$

where Δ is the forward difference operator, α_1 is a dynamic amplification factor, f_1^1 is an initial force approximation, and $\Delta \tilde{e}_1$ is a force increment which will provide the next force estimate as

$$f_2^1 = f_1^1 + \Delta \tilde{e}_1. \quad (\text{A.4})$$

At the first iteration, we have:

$$\Delta e_1 = f_2^1 - f_1^1 - \Delta \tilde{e}_1 \quad (\text{A.5})$$

$$\Delta e_1 = \Delta e_0 - \alpha_1 \Delta e_1. \quad (\text{A.6})$$

We can proceed similarly for the k th and $(k+1)$ th iterations. The largest eigenvalue of the iteration matrix can be approximated as $\lambda_1 \approx \tilde{e}_{k+1}/\tilde{e}_k$. Starting with the k th differences in f^1 values among consecutive subiterations, a geometric series is formed in terms of $\tilde{e}_k, \lambda_1 \tilde{e}_k, \lambda_1^2 \tilde{e}_k, \dots$ and the partial summation of diminishing geometric series for $|\lambda_1| < 1$ and $|\lambda_1| \neq 1$ is given by

$$\sum_{i=k}^{\infty} \tilde{e}_i = \frac{\tilde{e}_k}{1 - \lambda_1} \quad (\text{A.7})$$

where $\tilde{e}_k = \alpha_k e_k$. By setting the auxiliary sequence $\alpha_k = 1$ in the iteration process, Eq. (A.7) recovers to:

$$\sum_{i=k}^{\infty} e_i = \frac{e_k}{1 - \lambda_1} \quad (\text{A.8})$$

which can be written as the standard Aitken's Δ^2 process in the following form:

$$\sum_{i=k}^{\infty} e_i = (f_*^1 - f_k^1) = \frac{e_k}{1 - \lambda_1} \quad (\text{A.9})$$

where f_*^1 is the Aitken's extrapolation of the solution and f_k^1 is the approximation to the solution at the k th iteration. In this sequence transformation, we can further define a function which is continuous in a neighborhood of $\lambda_1, \lambda_1 \neq 1$ and satisfies

$$\gamma_1 = \frac{1}{1 - \lambda_1}. \quad (\text{A.10})$$

From the above error iteration analysis, we recover the standard kernel of Aitken's Δ^2 sequence transformation [50,53] which is regular and accelerates the convergence of linearly convergent sequences. In other words, the power series of Aitken's process is designed to eliminate only a single exponential term or the dominant eigenvalue. However,

this limitation can be removed by considering the iterated Aitken's Δ^2 process with sequential extrapolations. In the next appendix, we present a second order version of the sequence transformation for the interface force.

Appendix B. Second-order proof of interface force

We next present the second-order proof of our extrapolation procedure based on the auxiliary α -stabilization sequence and show that the ratio of recursive error sequence leads to the second largest eigenvalue λ_2 as

$$\left(\frac{\|\tilde{\mathbf{E}}_{k+1}\|}{\|\tilde{\mathbf{E}}_k\|} \right)^{(2)} = \lambda_2 \quad (\text{B.11})$$

after elimination of the first dominant eigenvalue λ_1 where $\Delta\tilde{\mathbf{E}}_k = \alpha_k \Delta\mathbf{E}_k$. Here superscripts (1) and (2) denote the first and second order approximations.

We assume that the interface force function possesses the convergent sequence and can be written as the partial sums through Taylor series arguments. The second-order error of the extrapolated force sequence \mathbf{f}_l can be written as the difference of first-order extrapolations with the aid of truncated linearly convergent sequences at k th and $(k+1)$ th:

$$\mathbf{f}_{*(k)}^{(1)} = \mathbf{f}_k + \gamma_1 \Delta\tilde{\mathbf{E}}_k^{(1)} + O(\|\Delta\mathbf{f}\|) \quad (\text{B.12})$$

$$\mathbf{f}_{*(k+1)}^{(1)} = \mathbf{f}_{k+1} + \gamma_1 \Delta\tilde{\mathbf{E}}_{k+1}^{(1)} + O(\|\Delta\mathbf{f}\|) \quad (\text{B.13})$$

$$\Delta\mathbf{E}_k^{(2)} = \mathbf{f}_{*(k+1)}^{(1)} - \mathbf{f}_{*(k)}^{(1)} + O(\|\Delta\mathbf{f}\|^2) \quad (\text{B.14})$$

$$\Delta\mathbf{E}_k^{(2)} = \Delta\tilde{\mathbf{E}}_k^{(1)} + \gamma_1 (\Delta\tilde{\mathbf{E}}_{k+1}^{(1)} - \Delta\tilde{\mathbf{E}}_k^{(1)}) + O(\|\Delta\mathbf{f}\|^2) \quad (\text{B.15})$$

where $\mathbf{f}_{*(k)}^{(1)}$ and $\mathbf{f}_{*(k+1)}^{(1)}$ denote the true solutions at the k th and $(k+1)$ th iterations, respectively. We can similarly write for $(k+1)$ th iteration:

$$\Delta\mathbf{E}_{k+1}^{(2)} = \Delta\tilde{\mathbf{E}}_{k+1}^{(1)} + \gamma_1 (\Delta\tilde{\mathbf{E}}_{k+2}^{(1)} - \Delta\tilde{\mathbf{E}}_{k+1}^{(1)}) + O(\|\Delta\mathbf{f}\|^2). \quad (\text{B.16})$$

At the k th iteration, the ratio of the norm of the error vector yields

$$\left(\frac{\|\Delta\tilde{\mathbf{E}}_{k+1}\|}{\|\Delta\tilde{\mathbf{E}}_k\|} \right)^{(2)} = \frac{\|\Delta\tilde{\mathbf{E}}_{k+1}^{(1)} + \gamma_1 (\Delta\tilde{\mathbf{E}}_{k+2}^{(1)} - \Delta\tilde{\mathbf{E}}_{k+1}^{(1)})\|}{\|\Delta\tilde{\mathbf{E}}_k^{(1)} + \gamma_1 (\Delta\tilde{\mathbf{E}}_{k+1}^{(1)} - \Delta\tilde{\mathbf{E}}_k^{(1)})\|}. \quad (\text{B.17})$$

In terms of eigenvalues λ and eigenvectors \mathbf{v} of the iteration matrix \mathbf{M} , we have the following power series:

$$\Delta\tilde{\mathbf{E}}_k^{(1)} = \sum_{i=1}^N c_i (\lambda_i)^k \mathbf{v}_i \quad (\text{B.18})$$

$$\Delta\tilde{\mathbf{E}}_{k+1}^{(1)} = \sum_{i=1}^N c_i (\lambda_i)^{k+1} \mathbf{v}_i \quad (\text{B.19})$$

$$\Delta\tilde{\mathbf{E}}_{k+2}^{(1)} = \sum_{i=1}^N c_i (\lambda_i)^{k+2} \mathbf{v}_i \quad (\text{B.20})$$

and then from Eq. (B.17) we obtain:

$$\frac{\|\Delta\tilde{\mathbf{E}}_{k+1}^{(1)} + \gamma_1 (\Delta\tilde{\mathbf{E}}_{k+2}^{(1)} - \Delta\tilde{\mathbf{E}}_{k+1}^{(1)})\|}{\|\Delta\tilde{\mathbf{E}}_k^{(1)} + \gamma_1 (\Delta\tilde{\mathbf{E}}_{k+1}^{(1)} - \Delta\tilde{\mathbf{E}}_k^{(1)})\|} = \frac{\left\| \sum_{i=1}^N c_i (\lambda_i)^{k+1} \mathbf{v}_i [1 - \gamma_1 (\lambda_i - 1)] \right\|}{\left\| \sum_{i=1}^N c_i (\lambda_i)^k \mathbf{v}_i [1 - \gamma_1 (\lambda_i - 1)] \right\|}. \quad (\text{B.21})$$

From the simplification of the right hand side of Eq. (B.21), the geometric extrapolation reduces the eigenvalues such that λ_2 becomes the dominant term with the quadratically convergent sequence as $\left(\frac{\|\tilde{\Delta E}_{k+1}\|}{\|\Delta E_k\|}\right)^{(2)} \approx \lambda_2$. Our current implementation confirms the second-order accuracy of the iterative force correction procedure.

References

- [1] R.D. Blevins, *Flow-Induced Vibration*, Van Nostrand Reinhold, New York, 1990.
- [2] B.M. Sumer, J. Fredsøe, Hydrodynamics around cylindrical structures, *Adv. Ser. Ocean Eng.* 26 (2006).
- [3] T. Sarpkaya, A critical review of the intrinsic nature of vortex-induced vibrations, *J. Fluids Struct.* 19 (2004) 389–447.
- [4] P.W. Bearman, Circular cylinder wakes and vortex-induced vibrations, *J. Fluids Struct.* 27 (2011) 648–658.
- [5] N. Jauvtis, C. Williamson, The effect of two-degree-of-freedom on vortex-induced vibration at low mass and damping, *J. Fluid Mech.* 509 (2004) 23–62.
- [6] C.H.K. Williamson, R. Govardhan, Vortex induced vibration, *Annu. Rev. Fluid Mech.* 36 (2004) 413–455.
- [7] J. Hron, S. Turek, A Monolithic FEM/Multigrid Solver for an ALE Formulation of Fluid–Structure Interaction with Applications in Biomechanics, Springer, 2006.
- [8] Y. Bazilevs, K. Takizawa, T.E. Tezduar, *Computational Fluid–Structure Interaction: Methods and Applications*, Wiley, 2013.
- [9] J. Liu, R.K. Jaiman, P.S. Gurugubelli, A stable second-order scheme for fluid–structure interaction with strong added-mass effects, *J. Comput. Phys.* 270 (2014) 687–710.
- [10] R.K. Jaiman, S. Sen, P. Gurugubelli, A fully implicit combined field scheme for freely vibrating square cylinders with sharp and rounded corners, *Comput. & Fluids* 112 (2015) 1–18.
- [11] C.A. Felippa, K.C. Park, C. Farhat, Partitioned analysis of coupled mechanical systems, *Comput. Methods Appl. Mech. Engrg.* 190 (2001) 3247–3270.
- [12] H.G. Matthies, R. Niekamp, J. Steindorf, Algorithms for strong coupling procedures, *Comput. Methods Appl. Mech. Engrg.* 195 (2006) 2028–2049.
- [13] R.K. Jaiman, P. Geubelle, E. Loth, X. Jiao, Combined interface condition method for unsteady fluid–structure interaction, *Comput. Methods Appl. Mech. Engrg.* 200 (2011) 27–39.
- [14] C. Farhat, K.G. van der Zee, P. Geuzaine, Provably second-order time-accurate loosely-coupled solution algorithms for transient nonlinear computational aeroelasticity, *Comput. Methods Appl. Mech. Engrg.* 195 (2006) 1973–2001.
- [15] F.J. Blom, A monolithic fluid–structure interaction algorithm applied to the piston problem, *Comput. Methods Appl. Mech. Engrg.* 167 (1998) 369–391.
- [16] C. Michler, E.H. van Brummelen, S.J. Hulshoff, R. de Borst, The relevance of conservation for stability and accuracy of numerical methods for fluid–structure interaction, *Comput. Methods Appl. Mech. Engrg.* 192 (2003) 4195–4215.
- [17] C. Forster, W.A. Wall, E. Ramm, Artificial added mass instabilities in sequential staggered coupling of nonlinear structures and incompressible viscous flows, *Comput. Methods Appl. Mech. Engrg.* 196 (2007) 1278–1293.
- [18] P. Causin, J.F. Gerbeau, F. Nobile, Added-mass effect in the design of partitioned algorithms for fluid–structure problems, *Comput. Methods Appl. Mech. Engrg.* 194 (2005) 4506–4527.
- [19] E.H. van Brummelen, Added mass effects of compressible and incompressible flows in fluid–structure interaction, *J. Appl. Mech.* 76 (2009) 02106.
- [20] S. Piperno, C. Farhat, Partitioned procedures for the transient solution of coupled aeroelastic problems part 1: Model problem, theory, and two-dimensional application, *Comput. Methods Appl. Mech. Engrg.* 124 (1995) 79–112.
- [21] W. Dettmer, Perić, A computational framework for fluid-rigid body interaction: finite element formulation and applications, *Comput. Methods Appl. Mech. Engrg.* 195 (2006) 1633–1666.
- [22] E.H. van Brummelen, Partitioned iterative solution methods for fluid–structure interaction, *Internat. J. Numer. Methods Fluids* 65 (2011) 3–7.
- [23] R.K. Jaiman, Advances in ALE based fluid–structure interaction modeling for offshore engineering applications, in: 6th European Congress on Computational Methods in Applied Sciences and Engineering, ECCOMAS 2012, Vienna, 2012.
- [24] R.K. Jaiman, M.K. Parmar, P.S. Gurugubelli, Added mass and aeroelastic stability of a flexible plate interacting with mean flow in a confined channel, *J. Appl. Mech.* 81 (2013).
- [25] R.K. Jaiman, F. Shakib, O.H. Oakley, Y. Constantinides, Fully coupled fluid–structure interaction for offshore applications, in: *ASME Offshore Mechanics and Arctic Engineering OMAE09-79804 CP*, 2009.
- [26] T.J.R. Hughes, A.N. Brooks, A multi-dimensional upwind scheme with no crosswind diffusion, in: *Finite Element Methods for Convection*, 1979, pp. 19–35.
- [27] A.N. Brooks, T.J.R. Hughes, Streamline upwind/Petrov-Galerkin formulation for convection dominated flows with particular emphasis on the incompressible Navier-Stokes equations, *Comput. Methods Appl. Mech. Engrg.* 32 (1982) 199–259.
- [28] T.J.R. Hughes, L.P. Franca, G.M. Hulbert, A new finite element formulation for computational fluid dynamics: Viii. The Galerkin/least-squares method for advective–diffusive equations, *Comput. Methods Appl. Mech. Engrg.* 73 (1989) 173–189.
- [29] J. Chung, G.M. Hulbert, A time integration algorithm for structural dynamics with improved numerical dissipation: the generalized- α method, *J. Appl. Mech.* 60 (1993) 370–375.
- [30] T.J.R. Hughes, W.K. Liu, T.K. Zimmerman, Lagrangian-Eulerian finite element formulation for incompressible visous flows, *Comput. Methods Appl. Mech. Engrg.* 29 (1981) 329–349.
- [31] J. Donea, Arbitrary Lagrangian-Eulerian Finite element methods, in: Belytschko T., Hughes T.J.R. (Eds.), *Computational Methods for Transient Analysis*, North-Holland, Amsterdam, 1983, pp. 474–516.
- [32] C. Johnson, *Numerical Solutions of Partial Differential Equations by the Finite Element Method*, Cambridge University Press, 1987.

- [33] K.E. Jansen, C.H. Whitting, G.M. Hulbert, A generalized-alpha method for integrating the filtered Navier–Stokes equations with a stabilized finite element method, *Comput. Methods Appl. Mech. Engrg.* 190 (2000) 305–319.
- [34] I. Harari, T.J.R. Hughes, What are C and h?: Inequalities for the analysis and design of finite element methods, *Comput. Methods Appl. Mech. Engrg.* 97 (1992) 157–192.
- [35] I. Akkerman, Y. Bazilevs, D. Benson, M.W. Farthing, C.E. Kees, Free-surface flow and fluid-object interaction modeling with emphasis on ship hydrodynamics, *J. Appl. Mech.* 79 (2012).
- [36] T.J.R. Hughes, L.P. Franca, M. Balestra, A new finite element formulation for computational fluid dynamics: V. Circumventing the Babuška–Brezzi condition: A stable Petrov–Galerkin formulation of the Stokes problem accommodating equal-order interpolations, *Comput. Methods Appl. Mech. Engrg.* 59 (1986) 85–99.
- [37] T. Tezduyar, S. Mittal, S.E. Ray, R. Shih, Incompressible flow computations with stabilized bilinear and linear equal-order- interpolation velocity–pressure elements, *Comput. Methods Appl. Mech. Engrg.* 95 (1992) 221–242.
- [38] T.E. Tezduyar, Finite elements in fluids: Stabilized formulations and moving boundaries and interfaces, *Comput. & Fluids* 36 (2007) 191–206.
- [39] M. Hsu, Y. Bazilevs, V. Calo, T. Tezduyar, T.J.R. Hughes, Improving stability of multiscale formulations of fluid flow at small time steps, *Comput. Methods Appl. Mech. Engrg.* 199 (2010) 828–840.
- [40] R. Jaiman, P. Geubelle, E. Loth, X. Jiao, Transient fluid–structure interaction with non-matching spatial and temporal discretizations, *Comput. & Fluids* 50 (2011) 120–135.
- [41] T. He, D. Zhou, Y. Bao, Combined interface boundary condition method for fluid-rigid body interaction, *Comput. Methods Appl. Mech. Engrg.* (2012) 81–102.
- [42] T. He, D. Zhou, Z. Han, J. Tu, J. Ma, Partitioned subiterative coupling schemes for aeroelasticity using combined interface boundary condition method, *Int. J. Comput. Fluid Dyn.* (2014) 1–29.
- [43] T. He, A partitioned implicit coupling strategy for incompressible flow past an oscillating cylinder, *Int. J. Comput. Methods* 12 (2015) 1550012.
- [44] R. Keedy, T.E. Tezduyar, S. Sathe, E. Stein, Space–time finite element techniques for computation of fluid–structure interactions, *Comput. Methods Appl. Mech. Engrg.* 195 (2006) 2002–2027.
- [45] U. Kuttler, W. Wall, Fixed-point fluid–structure interaction solvers with dynamic relaxation, *Comput. Mech.* 1 (2008) 61–72.
- [46] C. Michler, E.H. van Brummelen, R. de Borst, An interface Newton–Krylov solver for fluid–structure interaction, *Internat. J. Numer. Methods Fluids* 47 (2005) 1189–1195.
- [47] C. Michler, E.H. van Brummelen, R. de Borst, Error-amplification analysis of subiteration-preconditioned gmres for fluid–structure interaction, *Comput. Methods Appl. Mech. Engrg.* 195 (2006) 2124–2148.
- [48] R. Jaiman, X. Jiao, X. Geubelle, E. Loth, Conservative load transfer along curved fluid-solid interface with nonmatching meshes, *J. Comput. Phys.* 218 (2006) 372–397.
- [49] R. Jaiman, P. Geubelle, E. Loth, X. Jiao, Combined interface boundary conditions method for unsteady fluid–structure interaction, *Comput. Methods Appl. Mech. Engrg.* 200 (2011) 27–39.
- [50] A.C. Aitken, Studies in practical mathematics: The evaluation of latent roots and latent vectors of a matrix, *Proc. R. Soc. Edinburgh* (1937) 57–269.
- [51] D. Buoso, A. Karapiperi, S. Pozza, Generalizations of Aitken’s process for a certain class of sequences, *Appl. Numer. Math.* 90 (2015) 38–54.
- [52] B. Irons, N.G. Shrive, *Numerical Methods in Engineering and Applied Science*, John Wiley and Sons, 1987.
- [53] A. Sidi, *Practical Extrapolation Methods: Theory and Applications*, Cambridge University Press, 2003.
- [54] C. Breziniski, M.R. Zaglia, Generalizations of Aitken’s process for accelerating the convergence of sequence, *J. Comput. Appl. Math.* 26 (2007) 171–189.
- [55] C. Breziniski, M.R. Zaglia, Construction of extrapolation processes, *Appl. Numer. Math.* 8 (1991) 11–23.
- [56] Y. Saad, M.H. Schultz, GMRES: A generalized minimal residual algorithm for solving non-symmetric linear systems, *SIAM J. Sci. Stat. Comput.* 7 (1986).
- [57] S. Behara, S. Mittal, Parallel finite element computation of incompressible flows, *Parallel Comput.* 35 (2009) 195–212.
- [58] MPI Webpage, www.mpi-forum.org, Technical Report, 2009.
- [59] G. Karypis, V. Kumar, METIS: A Software Package for Partitioning Unstructured Graphs, Partitioning Meshes, and Computing Fill-Reducing Orderings of Sparse Matrices, Version 4.0, <http://glaros.dtc.umn.edu/gkhome/metis/metis/download>, Technical Report.
- [60] L. Smith, M. Bull, Development of mixed mode MPI/OpenMP applications, *Sci. Program.* 9 (2001) 83–98.
- [61] T.J.R. Hughes, G. Engel, L. Mazzei, M.G. Larson, The continuous Galerkin method is locally conservative, *J. Comput. Phys.* 163 (2000) 467–488.
- [62] H. Melbø, T. Kvamsdal, Goal oriented error estimators for Stokes equations based on variationally consistent postprocessing, *Comput. Methods Appl. Mech. Engrg.* 192 (2003) 613–633.
- [63] E.H. van Brummelen, K.G. van der Zee, V.V. Garg, S. Prudhomme, Flux evaluation in primal and dual boundary-coupled problems, *J. Appl. Mech.* 79 (2012) 010904–8.
- [64] C.G. Thomas, P. Nithiarasu, An element-wise, locally conservative Galerkin method for solving diffusion and convection–diffusion problems, *Internat. J. Numer. Methods Engrg.* 73 (2008) 642–664.
- [65] M. Zhao, L. Cheng, T. Zhou, Numerical simulation of vortex-induced vibration of a square cylinder at a low Reynolds number, *Phys. Fluids* 25 (2013) 023603(1)–023603(24).
- [66] C.H.K. Williamson, A. Roshko, Vortex formation in the wake of an oscillating cylinder, *J. Fluids Struct.* 2 (1988) 355–381.
- [67] A. Bokaian, F. Geola, Wake-induced galloping of two interfering circular cylinders, *J. Fluid Mech.* 146 (1984) 383–415.
- [68] G.R.S. Assi, P.W. Bearman, J.R. Meneghini, On the wake-induced vibration of tandem circular cylinders: the vortex interaction excitation mechanism, *J. Fluid Mech.* 661 (2010) 365–401.